Hydrophobic coating using sustainable sol-gel process doped with carboxylic acids to protect heritage copper artefacts

Silvia Lob, Delphine Neff, Thu-Hoa Tran-Thi, Maria Christine Richter, Charles Rivron

Title

Hydrophobic coating using sustainable sol-gel process doped with carboxylic acids to protect heritage copper artefacts

Authors

Silvia Lob[1,2], Delphine Neff[1], Thu-Hoa Tran Thi[2], Maria Christine Richter[3], Charles Rivron[2]

1 LAPA-NIMBE/IRAMAT, CEA, CNRS, Université Paris-Saclay, 91190 Gif-sur-Yvette, France

2 LEDNA-NIMBE, CEA, CNRS, Université Paris-Saclay, 91190 Gif sur Yvette, France

3 CY Cergy Paris Université, CEA, LIDYL, 91191 Gif-sur-Yvette, France and Université Paris-Saclay, CEA, LIDYL, 91191 Gif-sur-Yvette, France

Corresponding author

Silvia Lob: Silvia.lob@proton.me

Abstract

Metal corrosion and its mitigation using alkoxysilane based sol-gel coatings presenting specific properties are a matter of interest in many areas of applications, from industrial to cultural heritage materials. Thanks to their adhesive and coupling nature with different molecules and substrates, they show excellent results against aggressive environments. This study focuses on the protection of historical copper-based alloys. A tetramethyl orthosilicate-based (TMOS-based) sol-gel coating was doped with carboxylic acid compounds (heptanoic, octanoic and decanoic acids) recognized for their non-toxicity and their interesting corrosion inhibition properties on ancient corroded copper. The development of the coating and the basic understanding of the fundamental chemistry as well as the protection mechanism on the historical samples were studied. Contact angle measurements allowed to show that the resulting coating displayed a hydrophobic protection at the surface of the samples while its chemical composition was evaluated using thermogravimetric analysis, SEM-EDS and Raman spectroscopy. The porosity of the sol-gel matrix and the distribution of the acids in the porous silica network were then investigated by establishing nitrogen adsorption/desorption isotherms at liquid N_2 temperature. Examination of the sample's cross-section by SEM-EDS showed that the TMOS-based coatings doped with carboxylic acids penetrated up to 60% in depth in the corrosion layer of the ancient copper, while the Raman analyses showed that the acids formed organometallic complexes both at the surface and in the corrosion layer, leading to the protection of the metallic substrate against further corrosion.

Highlights

- Sol-gel synthesis with carboxylic acid was successfully used to coat ancient copper.
- Carboxylic acid complexes at the surface and in the corrosion layer, protecting it.
- Doped coating provides hydrophobic property to the surface of the copper.
- Carboxylic acid penetrates up to 60% of the corrosion layer thanks to silica matrix.
- Silica matrix displays a carboxylic acid reservoir for long term corrosion inhibition.

Keywords

Sol-gel, hydrophobic coatings, carboxylic acids, corrosion inhibition, cultural heritage, copper-based alloys.

1. Introduction

Metal corrosion and its mitigation have been investigated for many years and remain nowadays an open research field. It is of huge interest for an extended variety of applications, from industrial to artistic works, including cultural heritage materials. During the past decades, research turned towards sol-gel coatings, environmentally friendly and widely adaptable, that showed excellent results for metal corrosion protection against aggressive environments. The sol-gel process is a waste-free method. Its processing is usually at room temperature, thus minimizing the volatilisation or degradation of any organic compounds added to the protective coating. It is a liquid-precursor based process, allowing casting the coating in complex shapes without machining or melting. Sol-gel coatings act as a corrosion inhibition system for metallic substrates. It can be either a cathodic or anodic inhibition, or a hydrophobic-based protection, all stopping water from reacting with the atmospheric oxygen and the metal. In the first case, the protection is based on the chemical reaction between the inhibitor and the substrate while in the second case it is based on a physical barrier obtained from the interaction of the sol-gel matrix with the substrate. Wang et al. published an exhaustive review in 2009 on different types of sol-gel coatings used for corrosion protection of various metals [1]. The alkoxysilanes based sol-gels turned out to be the most widely used for corrosion protection, because of their adhesive and coupling nature with different molecules and substrates. To enhance the anti-corrosion properties of these coatings, the alkoxysilanes were organically modified to produce organic-inorganic hybrid gel materials (OIHs xerogels). OIH gel materials combine both the advantages of organic polymers (i.e., impact resistance, flexibility and lightweight) and the properties of inorganic material components (i.e., chemical resistance, thermal stability, and mechanical strength). The protectiveness of these OIH coatings was then provided by the barrier effect induced by the reaction of the siloxanes formed during the sol-gel process with the metallic substrate, and the inhibition role of the organic molecule crafted, or added by a doping method, to them [1,2]. Figueira and al. (2020), recently reviewed the most promising hybrid coatings to be used as active corrosion protection for metallic based substrates [3]. Most of them are based on organo-alkoxysilane precursors containing organo-functional groups, like epoxy [4–11], methacrylic [12,13], or vinyl [3] that can be polymerized to further increase the coating's density, and thus improving its physical barrier effect, forming a hydrophobic layer chemically bound to the metallic surface [4]. Regarding the doping process with corrosion inhibitors, the literature shows that it is mostly organic molecules such as tolytriazole and benzotriazole and inorganic cerium (Ce) salts that are to be used with an alkoxysilane based sol-gel [14–17]. On the one hand, the organic inhibitors act as cathodic inhibitors by suppressing the cathodic reduction reaction [14]. On the other hand, the Ce salts enhance the

corrosion resistance through a barrier effect, forming a passive oxide film over the metal surface [16][17].

Since the past decade an attempt was made to adapt sol-gel coatings for metallic cultural heritage purposes. In such context, corrosion protection issues are not only to preserve the metal, but also, the corrosion layer (CL) of the artefact. Thus, applying these coatings to highly complex material such as an old CL metal artefact proves to be a real challenge. Indeed, the material to be protected is itself a highly porous (with pores ranging from a few tens of microns to a few nanometres [18–20] and heterogeneous system, highly resistive, which makes the coating process all the more difficult. The conservation of cultural heritage presents an additional type of challenge due to its very specific requirements. The treatments developed must protect and last for many years, while presenting no aesthetical changes to the object, no toxicity for the environment or the human operator and generally involve a reversibility proceeding. Therefore, the sol-gel chemistry appeared an interesting choice, easy to synthesize and applicable on substrates with variable geometries. Alkoxysilanes based sol-gels were considered to coat metallic substrates because of their efficiency to form metallo-siloxane bonds on the metal surface, thus strengthening the surface adhesion of the coating to the surface. The production of sol-gel coatings with alkoxysilanes was well explained by Zucchi (in Corrosion and Conservation of Cultural Heritage Metallic Artefacts chapter 24), along with their application on outdoor bronze artefacts [21]. To act as an anti-corrosion coating, a functional group was added to the alkoxysilane, to play an inhibition role, lowering corrosion rates (acting on either the cathodic or anodic reaction, depending on the functional group chosen – the corrosion inhibitors for metallic heritage were well reviewed from Cano and Lafuente in 2013 [22]). In 2007, Joseph et al tested the triethoxitridecafluoroctyl silane as a hydrophobic protection coating for copper CL naturally aged [23]. They demonstrated its corrosion inhibition efficiency by electrochemistry impedance spectroscopy (EIS), tested over 8 months exposure under atmospheric conditions. The coated corroded copper showed an impedance value two orders of magnitude higher than the untreated one, illustrating the protection effect of the coating. After these first experiments, another study from Balbo et al (2012) investigated the protectiveness of a mercapto functionalized alkoxysilane, 3-mercaptopropyl-trimetoxysilane (PropS-SH) sol, deposited on a bronze substrate whose composition reproduces the microstructure of Renaissance leaded bronzes [24]. This preliminary study was conducted on the bare metal, submitted to both NaCl environment and acid rain. The polarization curves obtained via electrochemical measurements, all over a 10-day period, demonstrated that the functionalized xerogel film deposited on top of the metal reduced the cathodic reaction of oxygen reduction, leading to a passivation behaviour. PropS-SH xerogel coating of bronze substrate was then further investigated by Chiavari et al (2015),

with focus on the aging of the PropS-SH coating [25]. Natural exposure of the coated bronze samples was conducted over 13 months. An artificial aging was also applied to evaluate the coating resistance to UV radiation using a climatic chamber with a UV light source. The authors showed that PropS-SH-based coatings partially restricted the formation and evolution of corrosion products over 13 months exposure in a coastal town (Rimini, Italy). This was observed with SEM-BSE images and demonstrated by the analyses conducted on the runoff rain collected from the samples exposed outdoor. This analysis showed a decrease of the copper dissolution for the samples treated with the xerogel coating. Recently, Masi et al (2018 et 2019) tested ProS-SH for the protection of artificially aged copper and bronze with a focus on both the metal and its CL evolution [26][27]. The authors demonstrated the good adhesion of a thin film of about 300 nm of the xerogel coating on the CL surface. This coating protected the metal and the CL from corrosion as illustrated by the polarisation curves recorded after exposure to concentrated synthetic acid rain. After 30 days exposure, a marked J_{cor} reduction was observed on the coated sample in comparison to its performance at shorter immersion times yet presenting J_{cor} values indicating the ability to hinder both the cathodic and the anodic reactions of the corrosion process. Such results show an effective blockage of both oxygen reduction process and anodic alloy dissolution, thus demonstrating a significant protectiveness of the ProS-SH coating. This phenomenon was still observed after 30 days exposure to the concentrated synthetic acid rain even though the corrosion process was slightly accelerated then compared to the 1 h results [26]. With a complementary study using X-ray photoelectron Spectroscopy (XPS) aimed at investigating the coating-substrate interface, the authors studied the chemical interaction of silica with metal oxide species [27]. They determined a good reticulation of the coating with binding energies (BE) values indicating a main contribution of the Si-O-Si bonds. Furthermore, two BE values associated with the sulphur element (S) indicated two different contributions of the S species, one related to the S-Cu thiolate bond and one related to sulphate. Thus, this points toward a binding mechanism of the coating onto the metal essentially due to the formation of metal-thiolate bonds.

Another OIH xerogel coating was more recently developed by Kiele et al (2016), remaining in the area of metallic cultural heritage protection studies. The coating was applied on bronze and brass artefacts using tetraethyl orthosilicate (TEOS) coupled with a hydrophobic hexamethyl disilazane (HMDS) [28]. Experiments were conducted on bare metals. Surface analyses by SEM and AFM after 28 days of photochemical ageing under UV light at 40 W (UV daily exposure), showed that the thickness of the OIH hybrid coating diminished, though keeping the same original surface roughness. The high contact angles (about 130-140°) remained constant through time, indicating the presence of a hydrophobic layer at the surface of the metals after exposure. Moreover, the efficiency of this protective OIH hybrid coating against corrosion was tested with electrochemical measurements (corrosion currents). The

results indicated that resistance to corrosion was increased for the OIH coated samples, even though time exposure seemed to diminish the inhibition efficiency.

Last, in a more traditional approach, metallic artworks are usually treated with a corrosion inhibition solution. During the past decades, research was conducted on carboxylic acid compounds, recognized for their non-toxicity and their interesting corrosion inhibition properties [29–37]. Several carboxylic acids with 7 to 11 carbon (HCn, n corresponding to the number of carbon in the alkyl chain) were studied by Rapin et al. to evaluate their respective protection against corrosion on zinc and iron materials [38]. Their study revealed that the anti-corrosion effect of the carboxylic acid was increased as the alkyl chain length increased (based on this study from 7 to 11 carbon). This effect was corroborated later in multiple works [31,37,39,40]. The carboxylic acid HC10 was especially studied in the field of metal conservation. Rocca et al. (2001 et 2004) then Chiavari et al. (2004) demonstrated the efficiency of HC10 in a sodium solution (NaC10) for the protection of lead artefacts [41][42] [43]. In particular, the authors, at the light of electrochemical studies, concluded to the formation of a hydrophobic lead carboxylate layer at the surface of the metal, acting as a passivation layer thus responsible for corrosion inhibition. Later on, Hollner et al (2007) and then Milbled (2010), studied this same compound for the protection of archaeological objects using samples made of copper and copper alloys artificially corroded[33] [44]. The electrochemical measurements conducted by Hollner et al (carried out in an electrolyte containing ASTM corrosive water added or not with basic solutions of sodium decanoate) enlightened the formation of a hydrophobic and passivating copper carboxylate layer at the surface of the corroded metal, showing a behavior like the one obtained with lead artefacts. Finally, few years ago, Apchain (2018) tested the HC10 compound on a historical copper, naturally aged and corroded [45]. The study confirmed the hydrophobic protection of the copper CL due to the formation of copper carboxylates at the surface. The HC10 carboxylic acid amount and its penetration into the CL appeared to be crucial for the efficiency of protection to environmental exposure (UV, lixiviation) thanks to corrosion experiments in isotopic labeled media. A complementary electrochemical study of Donnici et al (2021) conducted on the same material showed a decrease of the cathodic reaction, thus allowing the authors to conclude to a corrosion inhibition property of these copper carboxylates formed at the surface of the CL [46].

Literature data clearly showed that carboxylic acids are efficient protection agents against corrosion for metallic artefacts. However, their application requires their dissolution in a solvent, and the immersion of the metallic artefact is time consuming and not suited for outdoor applications.

To address this matter, the present study proposes to adapt the carboxylic acid treatment using a silica xerogel as a reservoir matrix of the inhibitor agent. This work applies to copper-based artefacts, most often used for statuary and ancient monuments, sampling copper roof plates around 100 years old. The aim is to preserve the corrosion layer (CL) of these artefacts while stopping the metal corrosion. The study focuses on the efficacy of doped silica sol to improve the penetration of the carboxylic acid into the CL also to form a hydrophobic layer at the surface of the artefact. The ability of the carboxylic acids to react with copper ions in CL and form the protective species, copper carboxylates, is evaluated. It also examines the impact of the alkyl chain length of the carboxylic acid on these two parameters.

As CL is a complex, highly resistive material, filled with pores of multiple sizes over a layer of several tens of' micrometres thick, electrochemical measurements are not used to examine the coating's protective efficacy directly on the treated historical samples. Thus, a specific methodology is undertaken, using a multi-scale analytical approach to better understand the mechanisms and physicochemical interactions between the alkoxysilane-based xerogel, the carboxylic acid and the copper, investigating both the surface and the cross-section of the CL. Hydrophobic properties, coloration, and chemical composition of the surfaces are first assessed on a macro scale with thermogravimetric TGA, Scanning electron microscope coupled to Energy dispersive spectroscopy (SEM-EDS) and Raman spectroscopy. The investigation is then extended to the micro-scale, considering the TMOS-based xerogel and the inhibitor agent penetration into the CL using SEM-EDS and Raman spectroscopy on CL cross-sections.

In this study, we use tetramethyl orthosilicate (TMOS) as a silica precursor to produce a protective coating because of its ability to improve metal resistance to oxidation and acidic corrosion at different temperatures thanks to its resistance heat and chemicals. TMOS hydrolysis and condensation reactions are also easily adaptable by controlling the pH and temperature of the sol, thus allowing good control of the pore size of the resulting TMOS xerogel matrix [47][48]. In addition, we dope the TMOS xerogel with inhibitor agents, carboxylic acids with 7, 8 and 10 carbons. Such doped-TMOS xerogel are coated on 100 years old copper samples by dip-coating. This methodology gives a first insight on the interactions at a micrometric scale between the mineral phases constituting the CL and the TMOS xerogel doped with carboxylic acid. Thus allowing us to determine the modification of the CL properties after coating, bringing information about the physico-chemical behaviour of these layers.

2. **Experimental**

2.1. Materials

Carboxylic acids (HCn), heptanoic (HC7), octanoic (HC8) and decanoic (HC10) at 99% purity were purchased from SigmaAldrich®. The silicon precursor, tetramethyl orthosilicate (TMOS) at 99.8% purity, also came from SigmaAldrich®. The substrate to be studied was a 100 years old historical copper from the Saint Martin church's roof plates in Metz [49–51]. It displayed a corrosion layer composed of 2 copper phases: cuprite Cu_2O (5 µm thick - at the interface with the metal) and brochantite $Cu_4SO_4(OH)_6$ (about 50 µm thick) representative of copper's atmospheric corrosion [18][50][52]. These two characteristic layers are composed of two and three main elements: Copper (Cu), Oxygen (O) and Sulfur (S) with the corresponding elementary mass composition (normalized mass wt%) : 89%wt Cu and 11%wt O for cuprite, and 55% of Cu, 35%wt of O and 10%wt of S for brochantite [53]. The samples used were coupons of 1.5 cm^2.

To get the materials reference signals for the Raman spectroscopy (see section below), synthetic phases representative of the corrosion layer products (copper oxides, cuprite and brochantite) and the metallic organic complexes were synthetized in the laboratory. Brochantite was prepared at 60°C from 0,1M copper(II) sulphate and sodium hydroxide solutions at pH 8.0, following the modus operandi described by Kratschmer [54]. Copper carboxylate were synthetized using the *L.Robinet* method [55]. Carboxylic acids were solubilized in soda at 60°C for 1h adding then a solution of copper sulphate leading to the formation of the copper carboxylates that were later rinsed with water 3 times and dried for 24h at 60°C. The phases were authenticated by XRD analyses.

The TMOS-based coatings were prepared via the sol-gel process in a one-pot synthesis as follows. The Sol was synthetized using TMOS/acetone/HCn/H_2O with a molar ratio of 1/4/0.34/8. The Sol volume was 20 mL. To accelerate the hydrolysis and condensation of the silica precursor, the Sol was heated at 50°C for 40 to 80 minutes (depending on the chain length of the acid used). The heating time was optimized by following the Sol viscosity evolution and its gelation point. For each doping acid studied the gelation point was slightly different. To prevent any risks of the Sol's gelation during application, it was made 20 min prior to that point. For all doping acids HCn, this time corresponded to a range of viscosity between 2 and 4 mPa.s. The Sol was applied by dip-coating under controlled atmosphere, with a temperature of 20°C and relative humidity (RH) of 45%. The coupons were dipped for one minute, once or twice (-1d and -2d), with 10 minutes drying after each dip. Each Sol was applied on 3 samples for reproducibility study. After the dip, coupons were kept for 1 day at room temperature under atmospheric condition before analysis. This application produced coatings of around 1 to 4 µm

on the top of the surface as described in the results, depending on the HCn used for doping. In this study the HCn doped-TMOS Sol synthetized with HC7, HC8 and HC10 are respectively referred to as TC7, TC8and TC10 (TCn-Sol, n corresponding to the number of carbons in the carboxylic acid alkyl chain) for simplification. The non-doped TMOS Sol is referred to as TMOS-Sol. We also refer to TCn-coating when examining the coupon after both dipping and drying processes.

2.2. Analytical techniques

In this study, analyses were conducted examining both the surface and the cross-section of samples. Cross-sections were prepared from samples embedded in an epoxy resin (EpoFix, Struers) and cut with a precision diamond saw (Minitom; Struers). The cross-sections were ground with SiC paper (up to grade 4000) under water, and then polished with 1 µm diamond paste on a velvet disk. For all experiments an untreated sample (M ref) was used as reference. The coated coupons were characterized by contact angle measurements, spectro-colorimetry, optical microscopy, SEM-EDS, TGA, and Raman spectroscopy.

Colorimetric measurements were performed using a Konica Minolta spectrophotometer CM2600D in the range of 400 to 700 nm with a d/8 configuration and an 8 mm viewing aperture, equipped with Spectra Magic 3.5 software. Calibration of the instrument was performed with a white calibration plate CM-A415 (Minolta). Measurements were acquired with specular component included (SCI) and excluded (SCE), UV 0%, Illuminant D65, viewing angle 10° and three flashes auto-averaging mode. For each TCn-Sol examined, five measurements per coated coupon were performed on 4 and 5 coupons for the -1d and -2d respectively. SCE results were used as they seemed more appropriate for measurements on metal surfaces. The spectra of the data were processed according to the CIEL*a*b* color space where L* is brightness, a* is the red-green component and b* is the yellow-blue component (D65/10 CIE Illuminant/observer condition). The color differential (ΔE) was calculated by the formula: $\Delta E = \sqrt{((\Delta L^*)^2+(\Delta a^*)^2+(\Delta b^*)^2)}$.

The hydrophobicity of the coated coupons was measured using a contact angle meter with the sessile drop method and the SCA20 software. A 2 µL droplet of distilled water was used as the test fluid, with an average measurement of 3-droplet per sample (each droplet is taken on a different spot).

Thermogravimetric analysis (TGA) was carried out on 10 -15 mg of grounded powder obtained from scraping the surface of the coated coupon (corrosion layer and xerogel included). All

measurements were performed with a TGA 92-1750 from SETARAM under a 90 mL.min^{-1} flow of Synthetic Air and 10 mL.min^{-1} air balance flow. The temperature range used was the one described by Rao for the analysis of synthetic brochantite: 25 to 900°C at a heating rate of 10°C.min^{-1} with an isotherm at 100°C for 30 min [56].

Field emission scanning electron microscopy (SEM; JEOL SEM 7001F) was used to investigate the interfaces between the TCn coatings and the brochantite layer of the coupons processed in backscattered electron (BSE) and secondary electron (SE) modes. The SEM is coupled to a silicon drift detector to obtain the elemental composition by energy dispersive X-ray spectroscopy (EDS). The analyzes were performed at 10 kV with a current of 10 nA on metallized samples. Data acquisition and processing were performed using Aztec software (Oxford Instruments).

Raman analyses were carried out on an Invia Renishaw micro spectrometer equipped with a frequency- doubled Nd-YAG green laser (532 nm wavelength) and a high groove density grating (2400 g/mm) associated with a charge coupled device detector. The beam was focused using a Leica optical microscope at ×50 magnification. The lateral size of the beam was 1.2 µm and its probed depth was approximately 1 µm. The laser power was filtered to 0.1 mW to avoid damage to the corrosion products. The energy of the spectrometer was calibrated by setting the Raman line of a silicon wafer to 520.5 cm^{-1}. The spectra were acquired using Wire 3.4 software with a resolution of 2 cm^{-1} between 100 and 3700 cm^{-1}, a dwell time of 30 s and 5 accumulations. The reference spectra for synthetic brochantite and peak assignments were based on publications by Frost and Martens et al, showing a specific peak at 973 cm^{-1}[57][58]. For the TMOS, HCn, and CuCn reference spectra, the assignments were made based on previous studies. The characteristic peaks positions for each of these compounds are gathered in Table 1, Table 2 and Table 3. For the TMOS previous work by Sassi (2002) and Robinet [59][60] indicated the presence of characteristic peaks at: 490 cm^{-1}, 810 cm^{-1}, 978, 1012 cm^{-1}, at 1451 and 1462 cm^{-1} and at 2850, 2954-2995 cm^{-1}, respectively corresponding to, Si-O-Si stretching, Si movement in its tetrahedral oxygen cage, Si-OH, Si-CH_2 and CH_3, CH_2 stretching. For HCn, assignments were made from the article of Génin (2001) [61]. The main peaks of the acid are: those of the carboxyl group, at 598 and 609 cm^{-1} (symmetric and asymmetric COO bending), C-C stretching at 896 cm^{-1}, CH_3 rocking at 1061 cm^{-1}, symmetric and asymmetric CH_3 bending at 1436 and 1445 cm^{-1}, CO stretching at 1297 cm^{-1}, and CH_3 and CH_2 stretching at 2850-3000 cm^{-1}. For CuCn, the assignments were made based on the work of Doyle and Pereira [62][63]. The main peaks of CuCn are at 203, 242, 271 cm^{-1} and 359 cm^{-}1, corresponding to O-Cu-O stretching and O-Cu-O bending. For CuC7, four specific peaks were also detected at 162, 271, 383 and 469 cm^{-1}, but were not assigned. For CuC8, three specific

peaks are observed at 200, 239 and 280 cm^{-1}. For CuC10, its specific peaks are identified at 208, 236 and 290 cm^{-1}.

Table 1: TC7 coated coupon detected Raman peaks with assignment based on literature; for TMOS Sassi 2002 and Robinet [59][60]*, for HCn, F. Génin 2001* [61]*, and for (CuCn), A. Doyle and DC. Pereira* [62][63].

HC7	CuC7	TMOS reference	Assignment*	Reference
122 (m)				
	162 (mw)			
	203 (ms)		δ O-Cu-O	[56] [57]
	223 (vw)			
	242 (vw)		δ O-Cu-O	[56] [57]
276 (w)	271 (ms)		δ O-Cu-O	[56] [57]
	336 (m)			
362 (w)	359 (ms)		ν Cu-O	[56] [57]
	383 (ms)			
401 (w)				
		403 (w)	δ Si-O-Si	[53] [54]
452 (w)			$\rho_{//}$ CO_2	[55]
	469 (ms)			
		490 (vs)	δ Si-O-Si	[53] [54]
602 and 627 (w)	597 and 627 (vvw)		δs CO_2, δa CO_2	[55]
	666 (m)		ν Cu-O	[56] [57]
672 (vw)			$\rho_{\perp}$ CO_2	[55]
729 (vw)	732 (m)			
759 (w)				
	773 (vw)			
785 (vw)				
		810 (m)	Si movement in its oxygen tetrahedral cage	[54]
820 (m)				
845 (w) and 865 (m)	842 (m)		υ CC	[55]
890 (s) et 907 (w)	892 (m)	909 (m)	υ' CC	[55]
	916 (m)			
	947 (m)			
974 (w)	972 (w)			
		978 et 1012 (s)	ν Si-OH	[53]
998 and 1027 (w)	1006 (w) and 1024 (vw)		$\rho_{//}$ CH_3	[55]
1065 1075 (m)	1060 (s)		$\rho_{\perp}$ CH_3	[55]
1115 (m)	1114 (m)			
1180 (w)	1180 (w)			
	1200 (vw)			
1212 (vw)				
	1223 (vw)			
1304 (ms)	1301 (m)		(νC-O, δsCH_3)	[55]
	1324 (w)			
1415 1440 1458 (s)	1416 1441 et 1456 (s)		δs CH_3, δa CH_3	[55]
		1451 and **1462 (ms)**	ν Si-CH_2	[53]
1524 (w)	1525 (vw)			

1555 (vw)				
1659 (m)			υCC+υCC	[55]
1710 et 1765 (vw)			υC=O	[55]
1930 (vvw)				
2085 (vw)				
2328 (vw)				
		2340 (vw)		
2716 2731 (m)	2720 (w)			
2862 2874 2897 (vs)	2856 2882 2912 (vs)	2850 (vs)	νCH_3	[56]
2916 2937 2961 (vs)	2935, 2962 (vs)	2954 (vs), 2995 (ms)	νCH_2	[56]

Table 2: TC8 coated coupon detected Raman peaks with assignment based on literature; for TMOS Sassi 2002 and Robinet [59][60]*, for HCn, F. Génin 2001* [61]*, and for (CuCn), A. Doyle and DC. Pereira* [62][63].

HC8	CuC8	TMOS reference	Assignment*	Reference
	107 (m)			
	154 (m)			
	200 (s)		δ O-Cu-O	[56] [57]
	223 (w)			
	239 (w)		δ O-Cu-O	[56] [57]
	258 (s)			[56] [57]
271 (vw)				
	280 (w)		δ O-Cu-O	[56] [57]
295 (vw)				
317 (vw)				
	320 (s)			
	338 (m)			
347 (vw)				
	368 (s)		ν Cu-O	[56] [57]
		403 (w)	δ Si-O-Si	[53] [54]
403 (w)	406 (vw)			
	421 (w)			
	454 (m)		$\rho_{//}\ CO_2$	[55]
	480 (w)			
		490 (vs)	δ Si-O-Si	[53] [54]
	505 (vw)			
600 and 608 (vw)	598 and 609 (vvw)		$\delta s\ CO_2, \delta a\ CO_2$	[55]
	666 (ms)		ν Cu-O	[56] [57]
673 (vw)			$\rho_{\perp}\ CO_2$	[55]
725 (vvw)	729 (m)			
	754 (w)			
787 (vw)				
	799 (w)			
		810 (m)	Si movement in its oxygen tetrahedral cage	[54]
	830 (vvw)			
842 (s) and 870 (vvw)	844 (vw)		υ CC	[55]
	868 (w)			

896 et 910 (s)	896 (w)	909 (m)	υ' CC	[55]
	926 (m)			
	944 (m)			
971 (vvw)				
		978 et 1012 (s)	ν Si-OH	[53]
1003 and 1032 (w)	986 and 1027 (w)		$\rho_{//}$ CH_3	[55]
1065 1077 (m)	1061 (m)		$\rho_{\perp}$ CH_3	[55]
1116 (m)	1115 (m)			
1180 (w)	1178 (mw)			
1210 (vw)	1210 (vw)			
	1240 (w)			
1304 (ms)	1297 (ms)		(νC-O, δsCH_3)	[55]
	1401 1412 (m)			
1420 1439 1458 (s)	1436 1445 1469 (s)		δs CH_3, δa CH_3	[55]
		1451 and **1462 (ms)**	ν Si-CH_2	[53]
1516 (vw)	1514 (vw)			
1654 1663 (mw)			υCC+υCC	[55]
1694 and 1742 (vvw)			υC=O	[55]
1917 (vvw)				
2085 (vw)				
2318 (vvw)				
		2340 (vw)		
2708 2731 (m)	2719 2729 (w)			
2862 2874 2897 (vs)	2846 2882 2905 (vs)	2850 (vs)	νCH_3	[56]
2912 2937 2961 (vs)	2941, 2962 (vs)	2954 (vs), 2995 (m)	νCH_2	[56]

Table 3: TC10 coated coupon detected Raman peaks with assignment based on literature; for TMOS Sassi 2002 and Robinet [59][60]*, for HCn, F. Génin 2001* [61]*, and for (CuCn), A. Doyle and DC. Pereira* [62][63].

HC10	CuC10	TMOS reference	Assignment*	Reference
120 (m)	119 (w)			
	150 (w)			
	208 (w)		δ O-Cu-O	[56] [57]
230 (w)				
	236 (m)		δ O-Cu-O	[56] [57]
	290 (m)		δ O-Cu-O	[56] [57]
357 (w)				
	369 (m)		ν Cu-O	[56] [57]
		403 (w)	δ Si-O-Si	[53] [54]
397 (w)	403 (m)			
	436 (w)			
478 (vw)			$\rho_{//}$ CO_2	[55]
		490 (vs)	δ Si-O-Si	[53] [54]
	494 (vw)			
572 and 615 (vw)	623 and 647 (vw)		δs CO_2, δa CO_2	[55]
666 (w)	684 (mw)		ν Cu-O	[56] [57]
691 and 695 (vw)			$\rho_{\perp}$ CO_2	[55]
727 (vw)				

741 (vw)	739 (vw)			
	754 (vw)			
	775 and 795 (vw)			
		810 (m)	Si movement in its oxygen tetrahedral cage	[54]
836 (w)	839 (vvw)			
858 (vvw)	857 (vw)		υ CC	[55]
	878 (vw)			
891 and 907 (m)	890 and 909 (mw)	909 (m)	υ' CC	[55]
	949 (m)			
958 (vw)				
		978 and 1012 (s)	ν Si-OH	[53]
990 and 1003 (w)	991 and 1009 (vw)		$\rho_{//}$ CH_3	[55]
	1029 (w)			
1063 and 1076 (m)	1065 and 1123 (m)		$\rho_{\perp}$ CH_3	[55]
1123 (m)				
1180 (w)	1180 and 1196 (vw)			
1217 (vw)				
	1228 (vw)			
1282 (w)				
1298 (s)	1296 (m)		(νC-O, δsCH_3)	[55]
1353 and 1371 (w)	1348 and 1367 (vw)			
1410 1435 1462 (s)	1409 1438 1454 (s)		δs CH_3, δa CH_3	[55]
		1451 and **1462 (ms)**	ν Si-CH_2	[53]
1485 (w)	1488 (vw)			
1524 (w)	1522 (vw)			
	1540 (vw)			
1554 and 1561 (vw)	1561 (vw)			
1611 1640 (mw)			υCC+υCC	[55]
1687 1722 1767 (vw)	1719 1777 (vw)		υC=O	[55]
1909 (vvw)	1913 (vw)			
2179 (vw)	2185 (vw)			
		2340 (vw)		
2363 (vw)	2362 (vvw)			
2592 and 2611 (vw)	2592 and 2611 (vw)			
2649 and 2659 (vw)				
2709 2725 (m)	2721 2733 (w)			
	2755 (vw)			
2845 2858 2874 2883 2895 (vs)	2846 2882 2912 (vs)	2850 (vs)	νCH_3	[56]
2920, 2940 (vs)	2935, 2962 (vs)	2954 (vs), 2995 (m)	νCH_2	[56]

2.3. Thermodynamic modelling

The thermodynamic diagrams were drawn with the Geochemist's workbench package. The database used was the thermo.com.V8.R6. full database (GEMBOCHS.V2-Jewel.src.R6 03-dec-1996).

2.4. Porosity measurements

Porosity was studied using isothermal analysis examining N_2 adsorption and desorption at liquid N_2 temperature. Two models were used, the Brunauer, Emmet and Teller method (BET), and the Density Functional Theory (DFT). The instrument used was a Quantachrome Autosorb-1-LP-MP. The gas flow was set at 20 µmHg/min and the temperature was initially at 50°C and subsequently 150°C. For TMOS and TCn monoliths samples were ground to powders.

3. Results and discussion

3.1. Surface analyses: colorimetry and hydrophobic properties of the TCn-coated coupons

This first part focuses on the surface properties of the TCn-coated coupons to determine the impact of the TCn coatings on the colour change and the hydrophobicity of the historical CL. The colour of the coated surfaces was first investigated using colorimetric measurements. Coupons coated with TC7, TC8 and TC10 showed a relatively unchanged appearance compared to the uncoated coupon, as illustrated in Figure 1. The observations were made for one and two dip-coatings (-1d and -2d) and verified by the obtained dE* values, presented in Table 4 as follows.

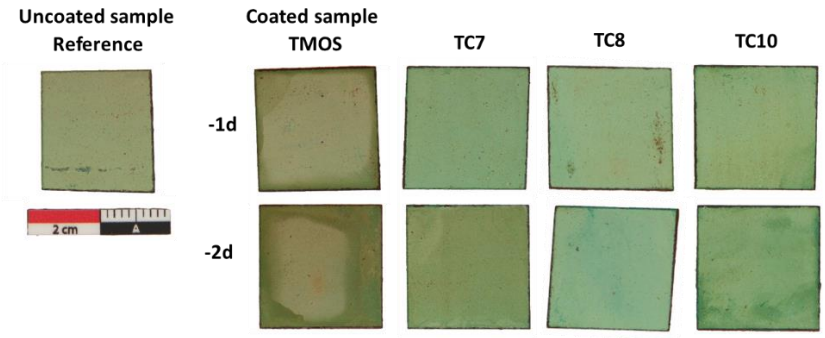

Figure 1: photograph image of the treated coupons TMOS, TC7, TC8 and TC10, -1d and -2d, compared to the untreated coupon (reference).

The measured dE* values for the TC7, TC8 and TC10 coated coupons (Table 4) were collected on 4 and 5 coupons for the -1d and -2d respectively. For the -1d coupons, the average dE* value was about 4.6 for TC7 and 3.6 for TC8, and about 5.8 for TC10. For -2d coupons, these values increased slightly for TC7 and TC8 coupons with values close to 5.5, while the gap in dE* -1d to -2d values were higher for TC10 (dE*~11). Nevertheless, the dE* values were relatively low and close to 5, implying an almost imperceptible change in colour at the surface,

as mentioned in several reviews [64][65]. It was also interesting to note the effect of the -2d, which seemed to increase the colour variation after treatment, especially for TC10.

Table 4: dE values for the coated coupons withTC7, TC8 and TC10, -1d (left) and -2d (right).*

	TC7		TC8		TC10	
coupon n°	**dE*(D65)**	**average dE***	**dE*(D65)**	**average dE***	**dE*(D65)**	**average dE***
1 dip-coating (-1d)						
1	3.9 ± 0.5	4.6 ± 0.5	3.9 ± 0.5	3.6 ± 0.5	4.9 ± 0.5	5.8 ± 0.5
2	4.7 ± 0.5		4.1 ± 0.5		5.7 ± 0.5	
3	4.6 ± 0.5		3.5 ± 0.5		6.5 ± 0.5	
4	5.2 ± 0.5		3.0 ± 0.5		6.2 ± 0.5	
2 dip-coating (-2d)						
1	5.6 ± 0.5	5.6 ± 0.5	6.8 ± 0.5	5.6 ± 0.5	8.8 ± 0.5	11.3 ± 0.5
2	6.3 ± 0.5		5.5 ± 0.5		10.9 ± 0.5	
3	6.2 ± 0.5		5.1 ± 0.5		8.3 ± 0.5	
4	5.4 ± 0.5		5.7 ± 0.5		14.0 ± 0.5	
5	4.3 ± 0.5		5.1 ± 0.5		14.5 ± 0.5	

It is also interesting to compare these results with the dE* values reported in another study by E.Joseph et al. (2007) [23], who also tested silane-based coatings functionalized with hydrophobic groups for artificially aged copper for cultural heritage conservation purposes. Our measured dE* show values very close to those reported in this work, which measured surface dE* of around 2 and 3.3 for the two preferred type of silane-based coatings tested. It is also remarkable that dE* remain quite low considering the addition of the carboxylic acid in the sol. Indeed, in a preliminary study performed by immersing the corroded samples directly in carboxylic acid solutions we noticed stronger dE* for all HC7, HC8 and HC10 with higher values from 5 for HC7, 8 for HC8 up to a maximum of 17 for the HC10 [66]. We can therefore advocate an improvement in colorimetric effect of TC7 and TC8 doped coatings.

Next, we examined the hydrophobic properties of TCn coated coupons to assess the water-repellence efficiency of TCn coatings. Contact angle (CA) measurements were performed on the surface of the TCn coated coupons exposed during 6 months to a controlled atmosphere at 60% relative humidity and 20°C (Figure 2). For each TCn, a set of 3 samples was analysed by measuring the CA of 3-droplets per sample.

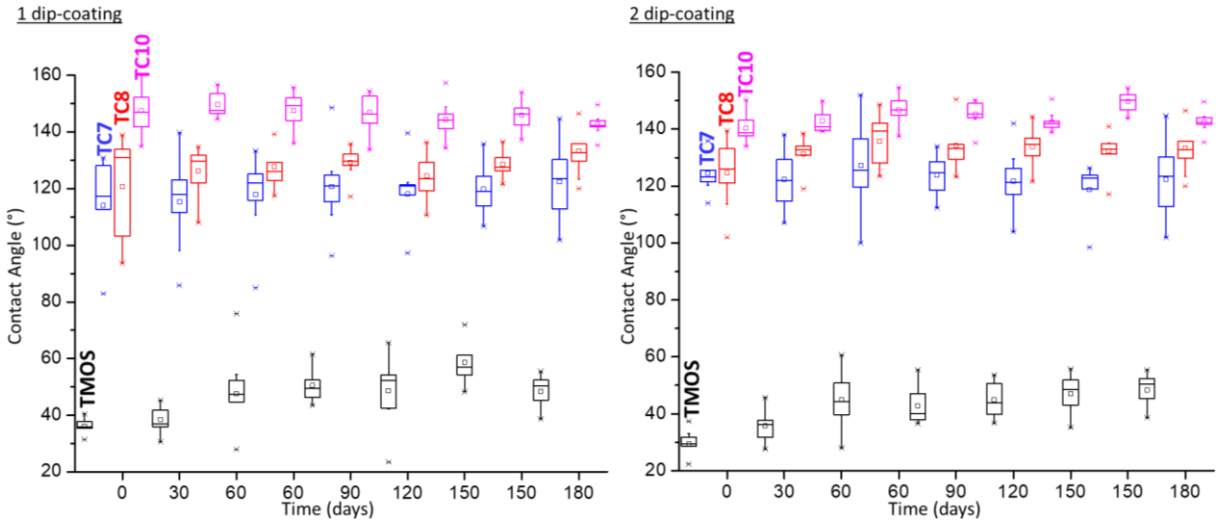

Figure 2: evolution of the contact angles (CA) measured for the coated coupons TMOS, TC7, TC8 and TC10, -1d (left) and -2d (right), exposed during six months to a controlled atmosphere at 60% relative humidity and 20°C, boxplot indicating the average, maximum, minimum, median and first and third quartile values.

For TC7-1d, TC8-1d and TC10 -1d coated coupons, the 6 months average CA values were above 120°. The average values for TCn-2d coated coupons were slightly higher over the 6 months, with a CA of 128° for TC7-2d, 137° for TC8-2d and 150° for TC10-2d. These results demonstrated that for all TCn coatings, both -1d and -2d, the CA values barely changed over time under these experimental conditions, showing only a slight decrease in average CA after 3 months. Figure 2 also showed that CA value varied with the length of the carboxylic acid alkyl chain, with higher CA for TC10 than TC8 and TC7. Thus, to evaluate the role of the carboxylic acid in the protective effect of the TCn coatings, these CA values were compared to those obtained for the coupon coated with undoped TMOS-Sol. The results showed that the undoped TMOS coating led to a hydrophilic surface of the coupon, illustrated in Figure 2 by the low average CA value over the 6 months of exposure at 40° observed for both -1d and -2d. Therefore, the carboxylic acid with long alkyl chain induced the water-repellency of the coating with an increase of hydrophobicity with the alkyl chain.

Again, we compared our results with previous work by Kiele et al. (2016) who measured CA values of 123° and 136° for methyl modified nano silica-coating used on artificially aged bronze samples before and after 28 days of artificial aging [28]. Once more, our TCn-coated coupons showed better hydrophobic performance that the siloxane-based coating tested. It is therefore worth emphasizing that TCn-coatings could represent a new type of siloxane coating to be considered for cultural heritage.

To complete the surface characterization, SEM-EDS analyses were conducted to determine the surface composition. The SEM electronic images obtained from the TCn coated coupons surfaces presented in Figure 3, showed that the external CL was covered with flower-shaped compounds. They appeared in dark grey on the SEM images. They were identified as copper

carboxylates (CuCn) by Raman analyses (presented in the Appendix A, Fig.A.1, Fig.A.2 and Fig.A.3). For TC7-1d, TC8-1d and TC10 -1d coated coupons (Figure 3 a,b,c) the coverage of the surface by these flower-shaped CuCn compounds increased with the carboxylic acid chain length as visible in the SEM images in Figure 3 a-c showing a larger coverage by dark grey shapes at their surface from a to c. The TCn-2d coated coupons (Figure 3 d,e,f) showed a higher coverage than the TCn-1d coupons, with a complete coverage observed for the TC10-2d. SEM images in Figure 3 d-f clearly illustrate this increased up to total coverage of the surface by the dark grey shapes representative of the CuCn. In both cases, CuCn compounds were present on the CL as an external element to the layer and their distribution was heterogeneous. This contrasts with the silica-based xerogel, which penetrated into the CL thus not leading to any observable deposition on top of the surface, as demonstrated later in the following paragraph on the examination of samples on cross-section (see 3.3).

The comparison of the TCn coated surfaces with the untreated coupon and the TMOS coated coupons, (Figure 4), clearly showed that these flower-shaped compounds were only formed on the TCn coated coupons. Indeed, the TMOS-1d coated coupon surface (Figure 4 j) appeared very similar to the one of the uncoated coupon (Figure 4 i), while the TMOS-2d coated surface (Figure 4 k) showed a very different aspect, with silica xerogel covering the entire CL, in tile-like aspect and displaying cracks all over the surface. These cracks can be the result of a too quick drying of the xerogel, since the undoped TMOS Sol condense quickly. Both EDX and Raman analyses conducted on the TMOS-1d and TMOS-2d coupons revealed the presence of silica xerogel at the surface (see Appendix B, Table B.1). No traces of CuCn were found (see Appendix B, Fig.B.1).

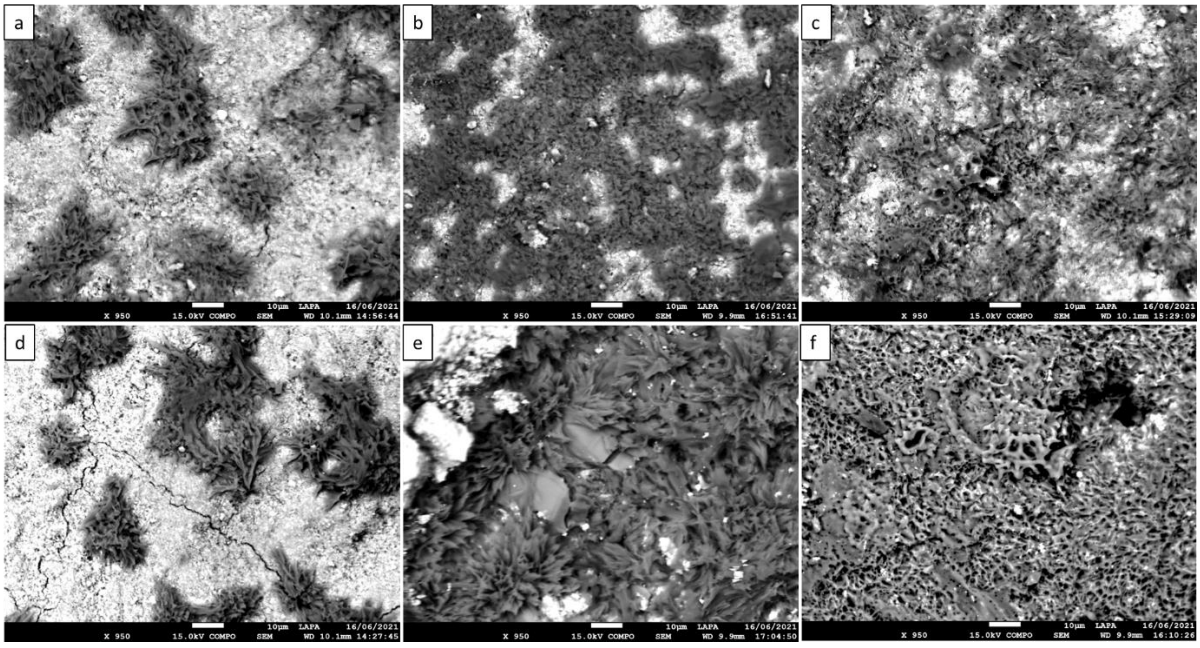

Figure 3: EDX electronic surface images of the coupons coated with TC7-1d and -2d (a and d), TC8-1d and -2d (b and e), and TC10-1d and -2d (c and f), scale 10 µm.

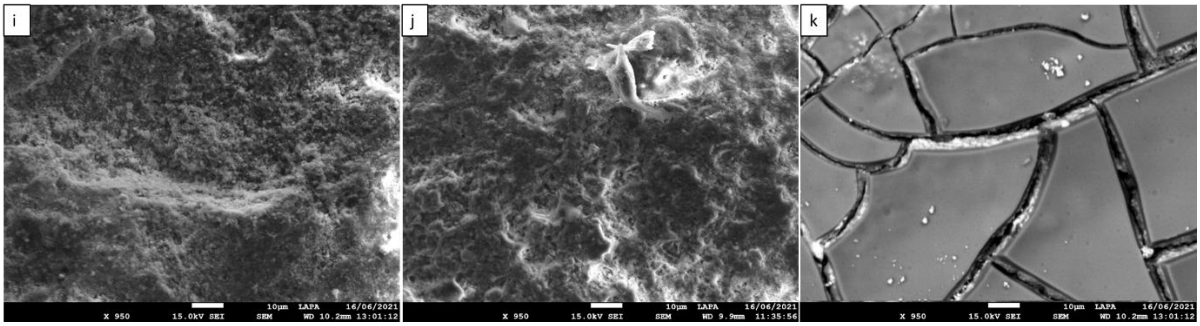

Figure 4: EDX electronic surface images of the uncoated coupon (i) and coupons coated with TMOS-1d (j) and TMOS-2d (k), scale 10 µm.

Linking this information with the surface hydrophobicity, it was possible to conclude that it was the flower shaped compounds, identified as CuCn, that were responsible for the hydrophobic protection of the TCn coated coupons.

3.2. Global chemical composition of the coupon's corrosion layer after TCn-coating

This section focuses on the chemical composition of the coated coupon's historical CL, TC7, TC8 and TC10. Thermogravimetric analyses (TGA) were used to determine the presence of brochantite, characteristic of the CL, TMOS, characteristic of the silica-based xerogel, and carboxylic acid, characteristic of the doping agent. All measurements were performed on powders obtained from scraping the surface of each coupon. These measurements were essential to establish the ability of the xerogel matrix to act as a carboxylic acid reservoir and to allow HCn molecules migration into the CL through the porous network. Figure 5 left shows the percentage of weight loss obtained as a function of the temperature (T) for the powders of uncoated TMOS, and TC7, TC8, TC10 coated coupons. A similar behaviour was observed for all coupons: i) a first large weight loss between 200 and 290°C, ii) a second weight loss between 290 and 450°C, iii) a third weight loss between 450 and 650°C, and iv) a fourth between 650 and 800°C. Thus indicating similar chemical compositions for all the CLs examined. The powders of the uncoated coupon and the TMOS coated coupon showed the same weight loss evolution, with an exact superposition of their curves, implying a large majority of brochantite and no detection of the SiO_2 network, probably due to its low concentration below the detection limit of the technique. The TC7 and TC8 coated coupon's curves overlapped, showing a slight increase in the overall percentage of weight loss compared to the uncoated and TMOS coated coupon's curves. A similar behaviour was observed for the TC10 coated coupon's curve, with an increased percentage of weight loss compared to the TC7 and TC8 curves. From the normalized decomposition plots of the weight loss (dw) over time variation (dt) versus temperature (T), it was possible to analyse these increasing weight losses between TC7, TC8 and TC10 coated coupons (Figure 5, right). The results first confirmed the weight loss data (%) on the uncoated and TMOS coated coupon powders, showing the same composition for both materials, as illustrated by the detection of

three main peaks identified at 380, 420 and 790°C and attributed to the thermal decomposition of the brochantite, as described in the literature.

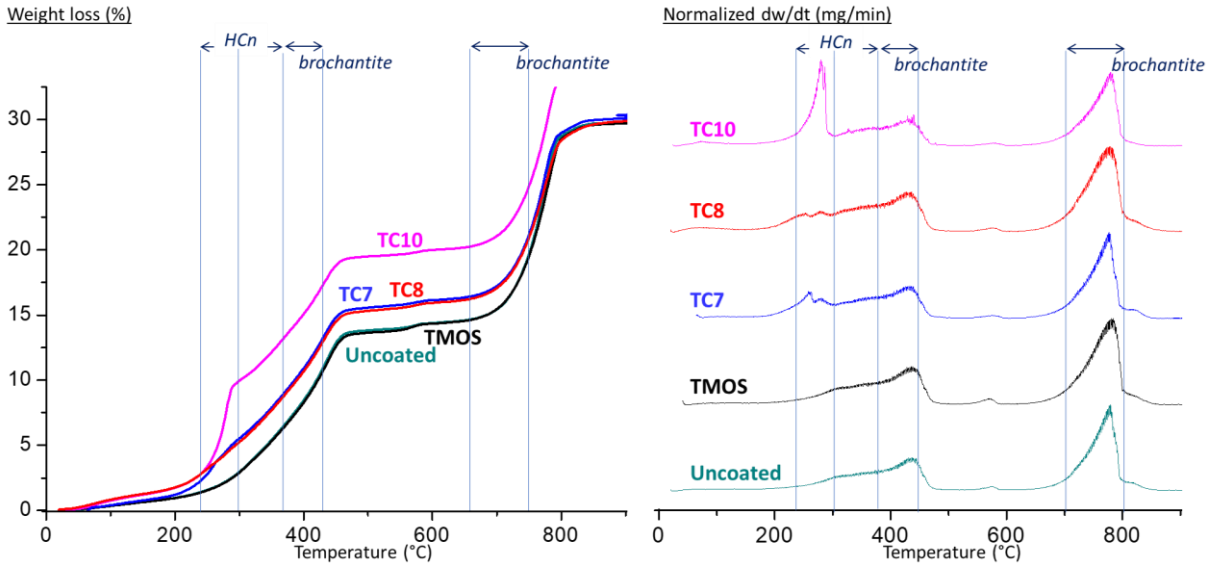

Figure 5: TGA graphs of powders of the uncoated coupon compared to the TMOS and TCn coated coupons with TMOS, TC7, TC8 and TC10; percentage of weight loss (left) and weight loss over time variation (dw/dt) (right) versus temperature.

Prasad et al (1984) and later Koga et al (1997) attributed these three peaks to antlerite ($Cu_3SO_4(OH)_4$) between 280 and 380°C, dolerophanite ($Cu_2O(SO_4)$) between 415°C and 550°C, and copper oxide (CuO) between 700°C and 800°C [67][68]. These results corroborate our previous data concerning the powders of TC7, TC8 and TC10 coated coupons. Indeed, the dw/dt of these coupons (Figure 5 right) revealed the presence of two additional peaks at 245°C and 340°C (HCn peaks in Figure 5 right), not detected for the powders scratched from the TMOS coated and the uncoated coupons. Both were attributed to the carboxylic acid compound, with the former attributed to the acid decarboxylation and the latter to the formation of oxygen-derived compounds [69]. However, peaks characteristic of thermal decomposition of TMOS were not detected, in any of the plots [56][69] [70]. These results are in agreement with previous TGA data on weight loss (%) and probably confirm a very low percentage of the TMOS-based xerogel in the CL compared to the other compounds, brochantite and carboxylic acid. From these TGA analyses, it was also possible to extract the percentage of acid (mass) contained in the CL, for all the TCn coated coupon powders, although this did not allow to differentiate the unreacted carboxylic acid (HCn) from its complex form (CuCn). The percentages of weight loss corresponding to the carboxylic groups and brochantite were compared and reported in Table 5 for all coupon's powders. For the TC7 and TC8, the weight loss corresponding to the carboxylic acid was about 9-10% by weight while it was slightly higher for the TC10, about 13%. These results demonstrated that the acid-doped xerogel was present both at the surface and in the CL.

Table 5: Mass decomposition of coupon's powders uncoated and TCn-coated; initial mass, decomposition products, temperature range and percent weight loss.

Coupon	Initial mass (mg)	Decomposition	Compound related	Temperature range (°C)	Weight loss %
uncoated	21.43 ± 0.02	antlerite	Brochantite	280-380	4.89 ± 0.04
		dolerophanite		415-550	4.41 ± 0.04
		copper oxide CuO		700-800	13.3 ± 0.04
TMOS	22.59 ± 0.02	antlerite	Brochantite	280-380	4.84 ± 0.04
		dolerophanite		415-550	4.44 ± 0.04
		copper oxide CuO		700-800	13.06 ± 0.04
TC7	22.27 ± 0.02	antlerite	Brochantite	280-380	5.09 ± 0.04
		dolerophanite		415-550	3.77 ± 0.04
		copper oxide CuO		700-800	11.73 ± 0.04
		acid decarboxylation	Carboxylic acid HC7	245	4.32 ± 0.04
		oxygen derived compounds		340	5.36 ± 0.04
TC8	21.01 ± 0.02	antlerite	Brochantite	280-380	5.1 ± 0.04
		dolerophanite		415-550	3.79 ± 0.04
		copper oxide CuO		700-800	11.31 ± 0.04
		acid decarboxylation	Carboxylic acid HC8	245	3.5 ± 0.04
		oxygen derived compounds		340	5.43 ± 0.04
TC10	22.47 ± 0.02	antlerite	Brochantite	280-380	5.93 ± 0.04
		dolerophanite		415-550	3.52 ± 0.04
		copper oxide CuO		700-800	12.03 ± 0.04
		acid decarboxylation	Carboxylic acid HC10	245	7.83 ± 0.04
		oxygen derived compounds		340	5.15 ± 0.04

Furthermore, still considering this system as a whole, it is worth mentioning briefly that we also studied the porosity of the system. However, we examined each component separately, for practical reason. The results are therefore not presented here, as they cannot be directly applied to the total system presented (the copper CL with the addition of the TCn coating). The TCn-coating porosity was investigated by examining the TCn-monolith using the BET method and DFT theory. The results obtained are presented in Appendix C, but the values were used only as a guide for pore volume size, bearing in mind that the TCn-monolith could not be directly assimilated to the pore size of the TCn-xerogel inside the CL. However, the study did enable us to compare the pore size of the TMOS-based xerogel as a function of the carboxylic acid used as reactant agent in the formulation (these data are discussed in more detail in the corresponding research[66]).

3.3. Cross-section analyses

This section focuses on the analysis of coupon cross-sections to assess the penetration and chemical reaction of TMOS-based Sols and carboxylic acids into the CL during the dip-coating process. These analyses were crucial in proposing, at a molecular level, a mechanism for carboxylic acid penetration and interaction in the CL via the TMOS-based xerogel porous

network. The interaction between HCn and the silica-based xerogel has not been considered as it has already been investigated in our previous study (when examining the molecular composition of the TCn-monolith by Raman analysis [66]). The results presented in Silvia Lob's corresponding PhD thesis demonstrated that HCn molecules remained trapped in the silica network filling its porosity but not chemically reacting with it. Since the Raman peaks detected in such material were those characteristics of TMOS and HCn only. TMOS characteristic peaks were detected at: 490 cm^{-1}, 810 cm^{-1} and 978 cm^{-1} respectively, corresponding to, Si-O-Si stretching, Si movement in its tetrahedral oxygen cage and Si-OH as explained in the experimental section [58][59]. For HCn, the main peaks detected were: those of the carboxyl group, at 598 and 609 cm^{-1} (symmetric and asymmetric COO bending), C-C stretching at 896 cm^{-1}, symmetric and asymmetric CH_3 bending at 1436 and 1445 cm^{-1}, and CO stretching at 1297 cm^{-1} [60].

To determine the CL stratigraphy and observe the presence of the TMOS-based xerogel, optical microscopy (OM) and scanning electron microscopy (SEM) were conducted on cross-sections. OM and SEM cross-section images of uncoated historical copper coupon, shown in Figure 6, distinguished the characteristic two-layer morphology of an atmospheric copper CL. The untreated CL consisted of cuprite at the interface with the metal about 5 µm thick (light grey brownish in optics Figure 6 left), and brochantite, on the top layer, about 40 µm thick (green blue in optics, Figure 6 left). This stratigraphy was based on the results of previous work [52][20].

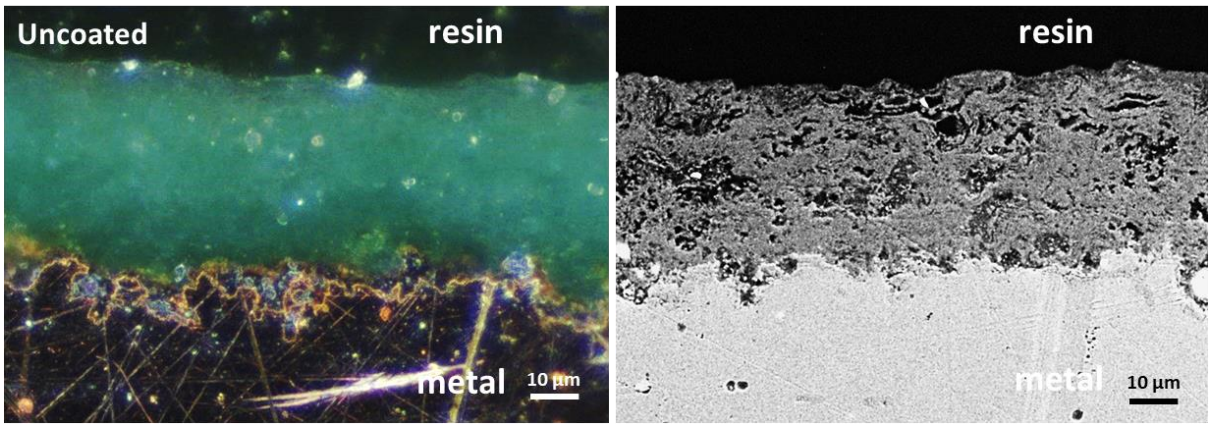

Figure 6: OM image (left) and SEM image (right) of the cross section of the uncoated coupon.

The stratigraphy of the uncoated coupon was then compared to that of the TCn coated coupons. For the undoped TMOS coated coupon, OM images of cross-sections showed the same two-layer morphology of the CL (Figure 7) as the uncoated coupon, a thin grey-brownish layer (OM) representing the cuprite at the interface with the metal and a thick blue layer (OM) for the brochantite up to the resin, indicating the preservation of CL integrity after coating. However, it was interesting to note that the -2d coated coupon had an additional layer on top

of the CL of approximately 2 µm thickness, illustrated by the white layer on top of the CL (Figure 7 right).

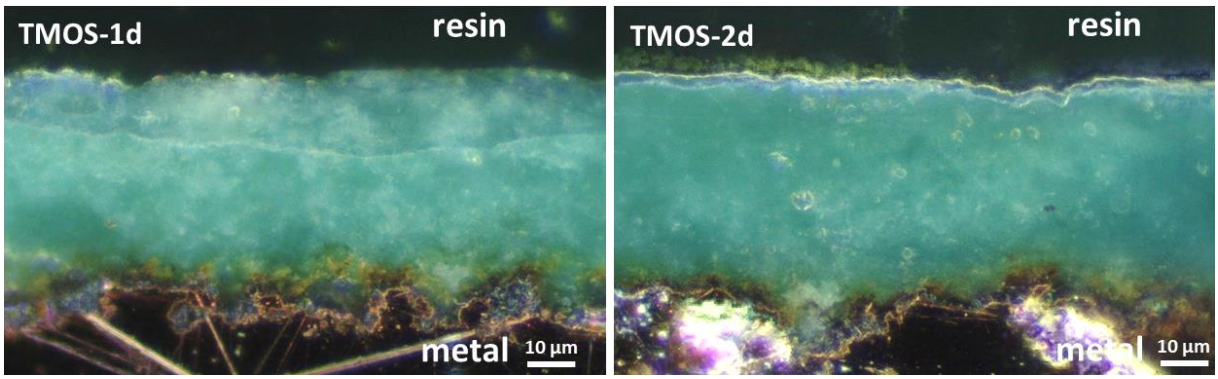

Figure 7: OM image of the TMOS treated coupon cross section, -1d (left) and -2d (right) with white spots in the metal due to a residue of silica from polishing.

Figure 8 displays a TC10 coated coupon for both the -1d and -2d. The OM images illustrated a similar layering of the CL as observed for the uncoated and TMOS-coated coupons, with a thin grey-brownish layer at the interface with the metal and a thick blue layer on top, up to the resin. But the TC10-2d cross-section (Figure 8 right) clearly showed an additional white layer deposition on top of the CL with a thickness of about 4 µm. It is important to note that these results were also representative of the TC7 and TC8 coated coupons, as presented in Appendix D (Fig.D.1 and Fig.D.2).

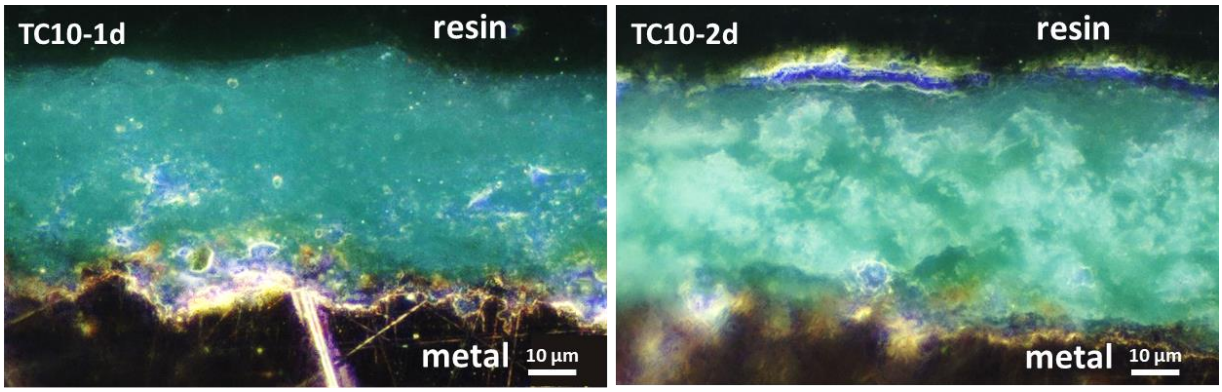

Figure 8: OM image of the cross section of the TC10 coated coupon, -1d (left) and -2d (right).

In addition, SEM-EDS analyses were performed on the cross-sections to further investigate the elemental composition of the CL and provide information on the nature of the thin film covering the CL and the penetration of the xerogel into the CL. They were evaluated with the detection of silica (Si) in the CL, characteristic of the TMOS-based xerogel. Electronic images and copper (Cu) mapping were used to delineate the CL area (represented by white dots in the SEM-EDS images), while Si mapping was used to determine the xerogel penetration.

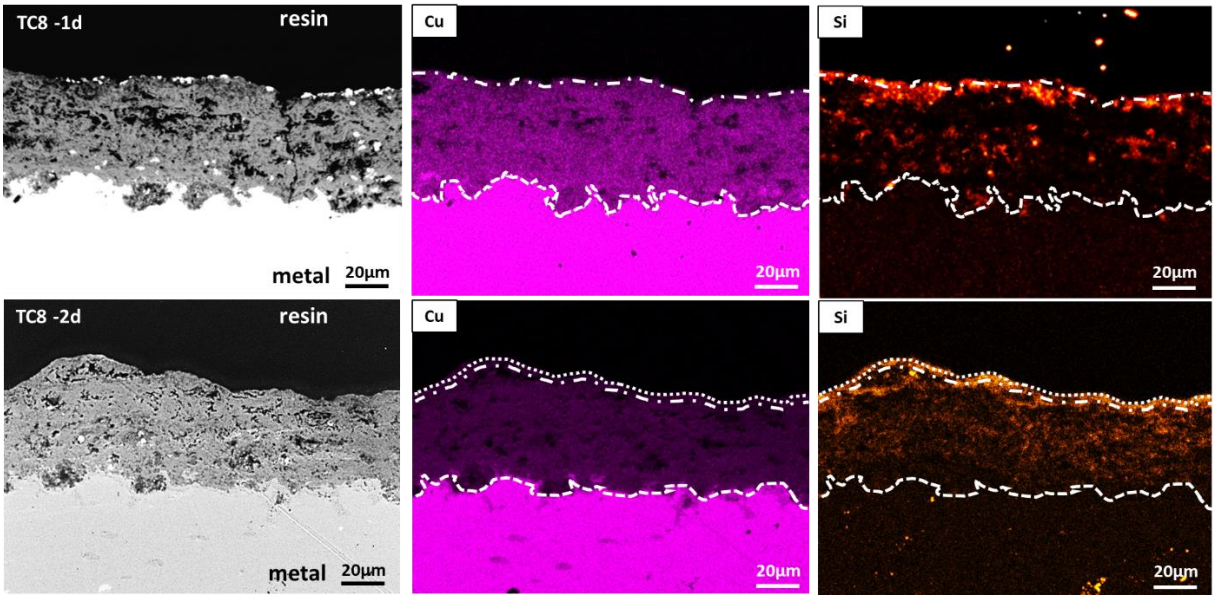

Figure 9: SEM image (left), Cu mapping (centre) and Si mapping (right) of the TC8 coated coupon cross section, -1d (top) and -2d (bottom).

For the TCn coated coupons, the observed stratigraphy presented the same organisation as previously observed on the OM: metallic copper at the bottom, a CL composed of cuprite (Cu_2O) and brochantite ($Cu_4SO_4(OH)_6$) and a resin layer on top, as illustrated in Figure 9 with the case of TC8 coated coupons. The distribution of Si in the CL (Figure 9 right) showed a region of high Si concentration at the surface (near the upper white dot lines) that then decreased with the penetration depth into the CL. No Si was observed in the cuprite layer at this observation scale, showing that this denser layer was not permeable to TMOS-Sol penetration. SEM-EDS mapping of the TC8-2d coated coupon (Figure 9 bottom right) showed a similar distribution of the Si penetration in the CL but also an additional Si layer deposited on top of the CL over approximately 2-3 µm. These results confirmed the observation made earlier by OMs (Figure 8 right). Again, it is important to note that these results were also representative of TC7 and TC10 coated coupons, displayed in Appendix E (Fig.E.1, and Fig.E.2). The stratigraphy results were compared to those obtained for the undoped TMOS coated coupons (Figure 10). Si mapping of the undoped TMOS coated coupon indicated a distribution of Si in the entire brochantite layer (Figure 10 right), as observed for the TCn coated coupons. This clearly demonstrates that the TMOS-Sol, with or without carboxylic acids, can penetrate the porous CL and that the carboxylic acids, when present, are trapped in the xerogel network when gelation occurs. The coating layer deposited on top of the CL was observed too, similarly to the TC8-2d coated coupon presented earlier, showing a denser Si layer above the CL (Figure 10 bottom right). In this case, the coating layer was cracked and thicker than the one measured on top of the TC8-2d coupon (about 6 to 8 µm). This result was not surprising since

in the absence of acids, the TMOS Sol condenses more quickly. Thus, leading to a Sol of higher viscosity, and a thicker coating that dries too quickly therefore cracking.

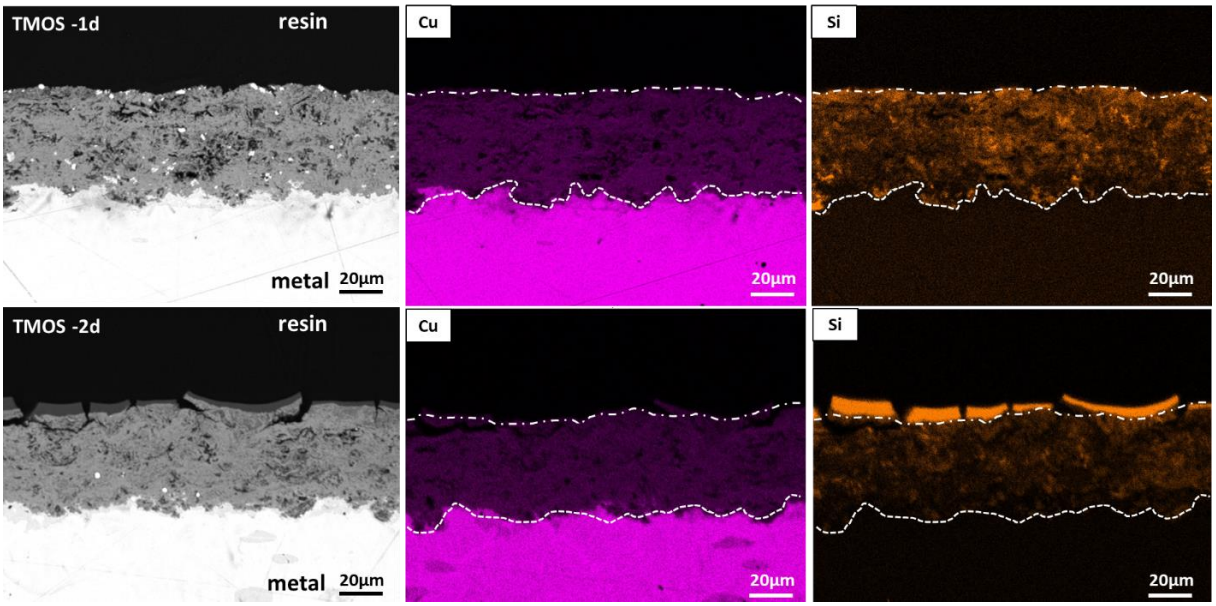

Figure 10: SEM image (left), Cu mapping (centre) and Si mapping (right) of the TMOS coated coupon cross-section, -1d (top) and -2d (bottom).

Next, we focused on the Si elemental mass percentage profiles (EDS profiles) of the coupon cross-sections to assess the depth of penetration of the xerogel into the CL. Before examining the results, it is important to point out that the CL prior coating already contains a certain amount of Si, independently of the xerogel. Measurements performed on the uncoated CL showed an average of 2.5 % wt Si in the CL [19,50,71,72]. Thus, only the Si content above the 2.5%wt limit was considered to evaluate the xerogel penetration in the CL. For all EDS profiles, the resin was shown on the left (high carbon (C) rates), the CL in the centre with brochantite ($Cu_4SO_4(OH)_6$) and cuprite (Cu_2O) (distinction of the two layers made by the sulphur (S) on oxygen (O) ratio), and the metal on the right (copper, Cu). The Si profiles of the TCn coated coupons displayed an interesting evolution as a function of the depth of penetration into the CL, as illustrated with the case of the TC8 in Figure 11 (orange line, Si relative mass%). These observations were also representative of TC7 and TC10 coated coupons (see profiles presented in Appendix F, Fig.F.1, and Fig.F.2). Thus, the Si profile of the TCn coated coupons could be divided in four regions:

- Z1: corresponding to the cuprite layer of the CL, at the interface with the metal, showing no trace of Si, meaning no TMOS-based xerogel in this interfacial layer.
- Z2: corresponding to the brochantite layer containing the xerogel, indicating the limit of the xerogel penetration into the CL. This limit was set as the depth in the CL at which the Si %wt falls below 2.5 %wt, corresponding to the Si %wt measured in the untreated CL.

- Z3: corresponding to the upper part of CL (at the interface with the resin); this region contains a higher concentration of xerogel than Z2 and was set to 10 µm in order to measure and compare the increase of Si in this region from sample to sample, due to the heterogeneity of the CL.
- Z4: corresponding to the Si coating deposited on top of the CL. It was determined by the Si %wt peak above the CL, and only detected for the -2d coatings.

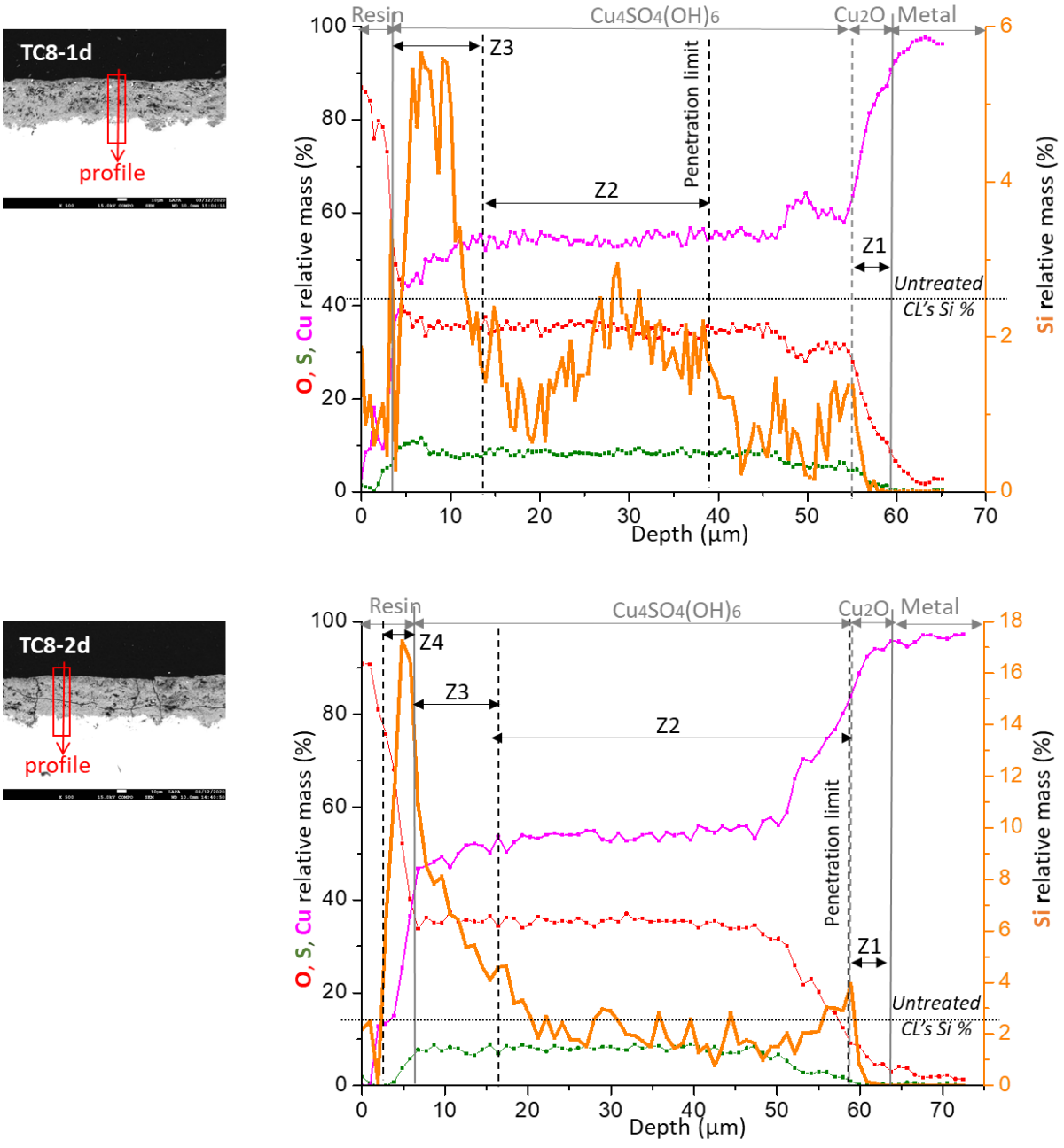

Figure 11: SEM EDS elemental profile lines for O, S, Cu and Si (scale on right side), in relative mass % correlated to the Si depth penetration in the CL for the cross section of the TC8 coated coupon, -1d (top) and -2d (bottom).

The Z2 and Z4 regions were examined in terms of the penetration of the TCn-Sols as a function of Z2 depth and Z4 thickness, for all TCn -1d and -2d coated coupons. The Si penetration

depth was calculated as a percentage of the entire CL thickness. The thickness of the Si coating, formed only for -2d, was evaluated by measuring the top layer above the CL. These values, reported in Table 6, exhibited Si penetration into the CL of about 57± 2.5% and up to 71± 9.8%, for all TCn -1d and -2d, indicating that the carboxylic acid chain length and the number of dip-coatings did not impact this penetration depth factor. While for the TMOS-1d and -2d, these Si penetration values were higher, of 73± 5.1% and 76± 4.8%**,** indicating that the addition of the acid into the Sol diminished the penetration depth of the Si into the CL. Moreover, the Si coating thickness of Z4 in Table 6 increased as the alkyl chain became longer: TC10 > TC8 > TC7 Si coating, indicating that the carboxylic acid chain length had however an impact on the coating thickness.

Table 6: Si coating thickness (Z4), Si depth's penetration (µm) (Z2) and penetration percentage from the entire CL, for the TCn coated coupons, -1d and -2d.

		Z4	**Z2**			
Coupon	Profile	**Si coating** on top of the CL (µm)	**Si penetration limit** into the CL (µm)	**CL thickness** (µm)	**Si depth penetration** into the CL (%)	
	n°		***1 dip-coating (-1d)***		*per profil*	*average per coupon*
TMOS	1	_	36	52	69	73 ± 5.1
	2	_	40	51	78	
	3	_	35	50	70	
TC7	1	_	27	48	56	57 ± 2.5
	2	_	30	50	60	
	3	_	26	47	55	
TC8	1	_	30	50	60	71 ± 9.8
	2	_	35	45	78	
	3	_	38	50	76	
TC10	1	3	25	45	56	64 ± 8.0
	2	2	35	49	71	
	3	2	30	46	65	
			2 dip-coatings (-2d)		*per profil*	*average per coupon*
TMOS	1	10	33	47	70	76 ± 4.8
	2	7	38	49	78	
	3	9	38	48	79	
TC7	1	1	30	50	60	63 ± 4.6
	2	1	35	57	61	
	3	2	37	54	69	
TC8	1	3	35	55	64	66 ± 2.2
	2	1	38	58	66	
	3	3	32	47	68	
TC10	1	4	25	40	63	65 ± 7.03
	2	3	35	48	73	
	3	3	25	42	60	

In what follows, we investigate the penetration of Si into the CL in the Z2 and Z3 regions. The Si/(Si+Cu) ratio was calculated to provide information on the Si concentration versus its

penetration depth for all TCn-Sols. The results displayed in Table 7 highlighted the higher concentration of Si in the upper CL (Z3) as observed in the EDS profiles. For all TCn coated coupons, the Si/(Si+Cu) ratio was always higher in the Z3 region than in the Z2 and CL (Z1+Z2+Z3). This indicated that the TMOS-based xerogel preferentially penetrated the upper part of the CL (Z3). For the undoped TMOS coated coupon, an equal Si penetration throughout the CL was observed (Table 7). Thus, comparison of these results established that the addition of the carboxylic acid to the TMOS-based Sol limited the amount of Si penetrating into the CL. Furthermore, the comparison of TCn -1d and -2d coated coupons, clearly showed that -2d led to an increase in Si concentration as compared to -1d in the Z3 region, regardless of the length of the alkyl chain. This result indicated that the number of dip-coatings increased the total amount of TMOS-based Sol penetrating the CL of Z3.

Table 7: Si/(Si+Cu) ratio (%) calculated in the Z3 (10 first µm of the CL) and Z2 (penetration limit into the CL) regions, for the Tcn coated coupons, -1d and -2d.

	Z3		**Z2**	
	Si/(Si+Cu) ratio (%) 10 first µm of the CL		**Si/(Si+Cu) ratio (%)** Si limit penetration in the CL	
Coupon	*1d-*	*2d-*	*1d-*	*2d-*
TMOS	31	33	33	29
TC7	17	23	13	15
TC8	18	24	13	16
TC10	18	29	18	16

Since HCn acids were brought in via the TCn-Sols, it was important to know the distribution of HCn and the nature of its interactions with the surrounding environment in the different regions Z2, Z3, Z4 where TMOS-based xerogel was found. In particular, an important question was: depending on the pH of the medium, is HCn present in a protonated or deprotonated form, or does it react with brochantite with formation of the CuCn complex. To answer, micro-Raman spectroscopy was used on cross-sections in order to determine the HCn molecular distribution. The compounds identification was based on several works of Sassi et al (2002) [59], Robinet [60], Génin et al (2001) [61], Doyle et al and Pereira et al [62][63]. The characteristic peaks were listed in Table 1, Table 2 and Table 3, presented earlier in the methodology section.

Raman spectra of the Z2, Z3 and Z4 regions obtained for TC7, TC8 and TC10, -1d and -2d coated coupons, (Figure 12, Figure 13 and Figure 14) displayed a similar distribution of the respective compounds (Si of TMOS, HCn, CuCn) into the CL. For TC7-1d coated coupon, two main types of spectra were distinguished (Figure 12). The Z2 and Z3 regions were mainly characterized by brochantite and a mixture of xerogel and carboxylic acid HC7 as shown in

spectra 1 on Figure 12. The Z3 area was characterized by the additional presence of copper carboxylate CuC7 as illustrated in *spectra 2* (Figure 12) showing its main peaks at 203, 242, 271 cm^{-1} and 359 cm^{-1} , corresponding to O-Cu-O stretching and O-Cu-O bending, as well as peaks at 162, 271, 383 and 469 cm^{-1}, which were not assigned (Table 1). These results indicated that Z3 region contained carboxylic acid as well as precipitated CuC7 in the CL porosity. For TC7-2d coated coupon, three main types of spectra were distinguished (Figure 12). For Z2 and Z3 regions the spectra were the same as those observed for coupon TC7-1d (*spectra 1 and 2* Figure 12). In addition, the Z4 region, corresponding to the Si coating on top of the CL, was characterized by both copper carboxylate CuC7 and carboxylic acid HC7, as well as traces of the TMOS-based xerogel as shown *in spectra 3* (Figure 12). Z2, Z3 and Z4 peaks for TC7-2d coated coupon were previously listed in Table 1.

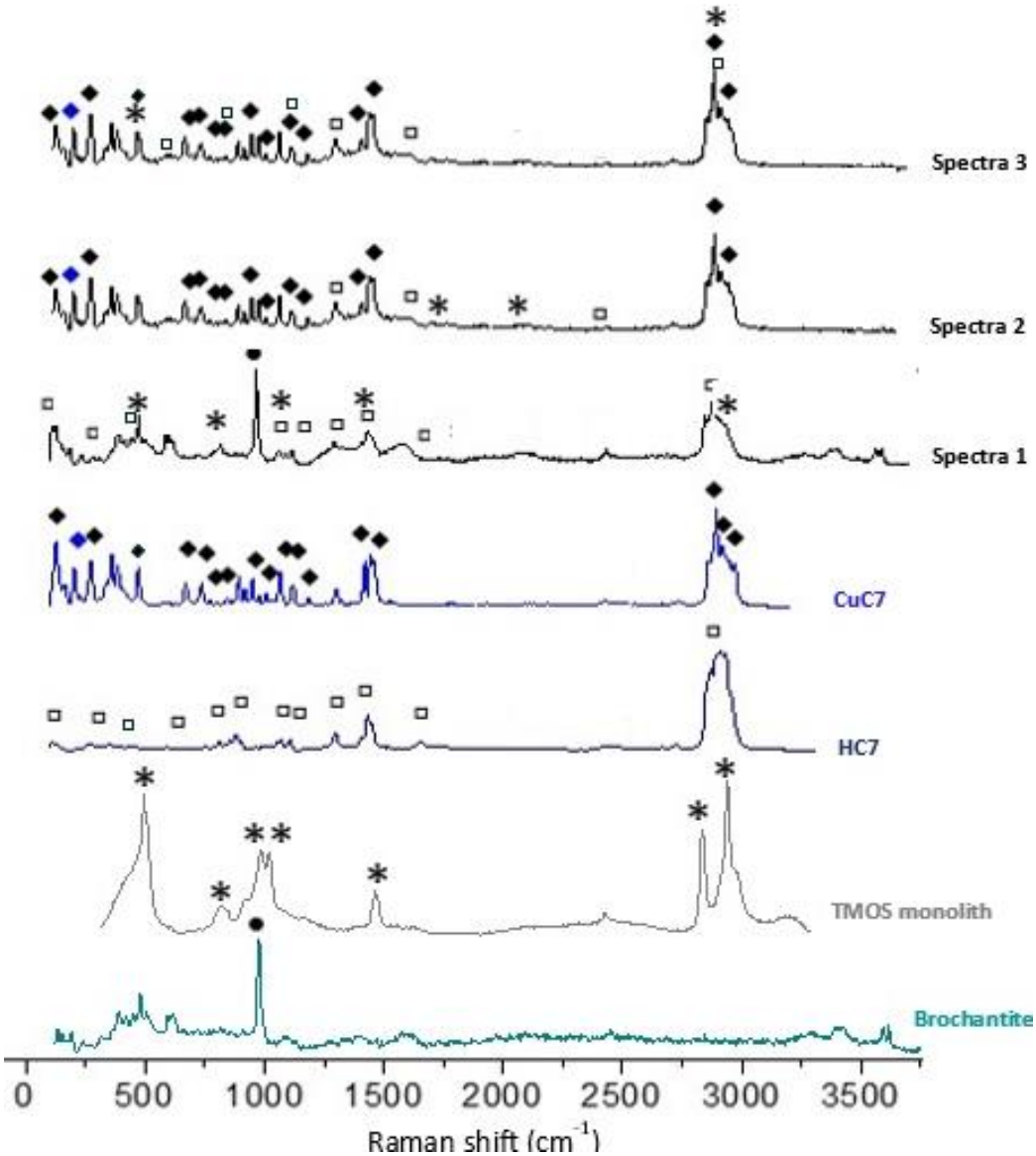

Figure 12: Z2 (spectra 1), Z3 (spectra 1 and spectra 2) and Z4 (spectra 3) characteristic Raman spectra for the treated coupon TC7 -1d and -2d cross-section.

For TC8 and TC10 -1d and -2d coated coupons (Figure 13 and Figure 14), the observations were similar. For both -1d and -2d coated coupons, Z2 and Z3 regions were characterized by a mixture of TMOS xerogel and carboxylic acid, in addition to brochantite already present in the uncoated coupon CL (*spectra 1* Figure 13 and Figure 14*).* The Z3 region was characterized by the additional presence of copper carboxylate CuC8 or CuC10 (*spectra 2* Figure 13 and Figure 14, showing their specific peaks at 200, 239 and 280 cm^{-1} and 208, 236 and 290 cm^{-1} respectively. For the -2d coated coupons, the Z4 region corresponded clearly to a mixture of CuCn/HCn, along with traces of TMOS-based xerogel (*spectra 3* Figure 13 and Figure 14 and peaks reported in Table 2 and Table 3). Therefore, for all TCn coatings, the phase distribution indicated a heterogeneous layer for Z2 and Z3 regions made of brochantite, TMOS-based xerogel and carboxylic acid, both unreacted (HCn) and complexed (CuCn), and a Z4 region corresponding to the TMOS-based xerogel containing the carboxylic acid, also present in its unreacted and complexed forms.

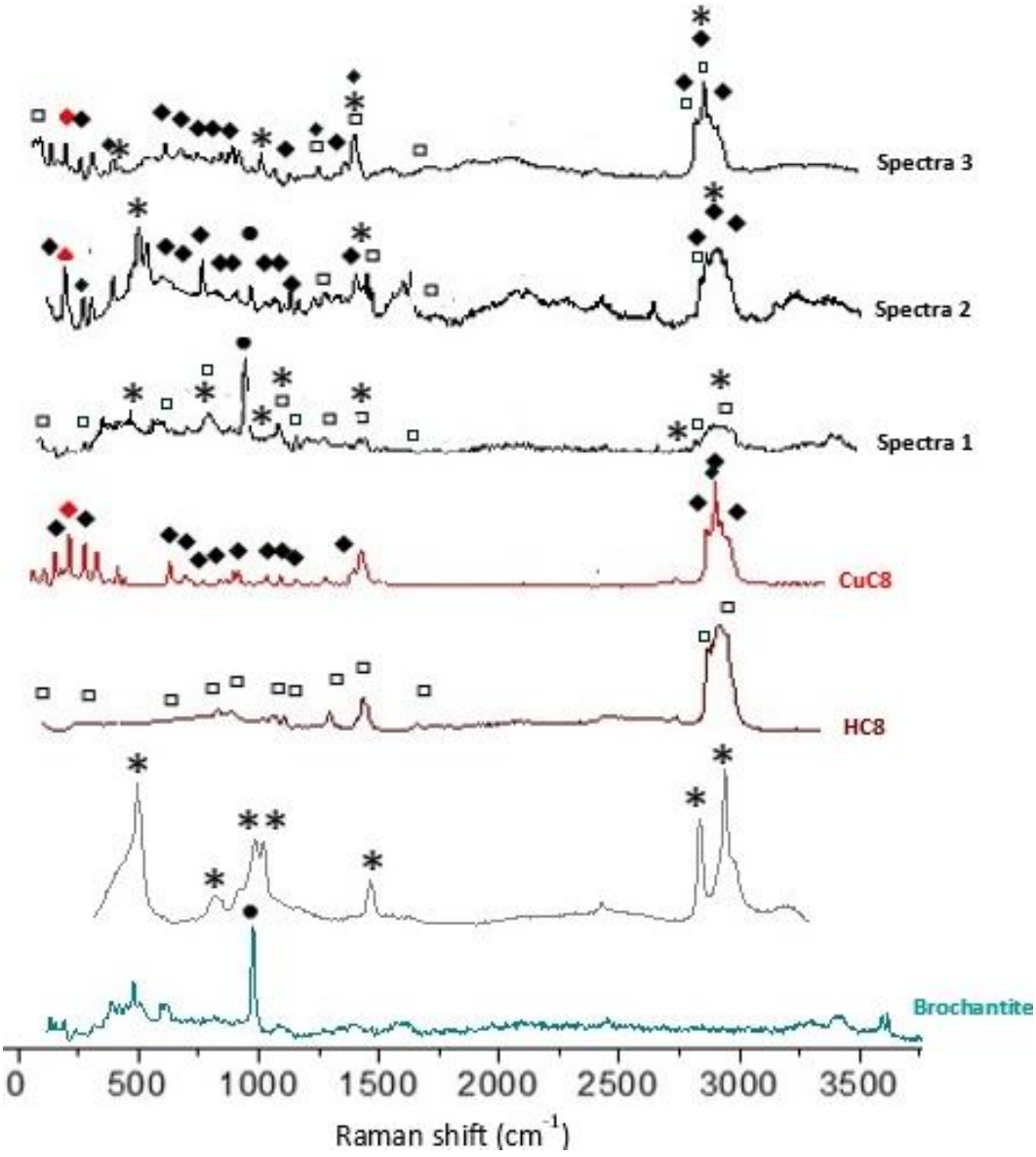

Figure 13: Z2 (spectra 1), Z3 (spectra 1 and spectra 2) and Z4 (spectra 3) characteristic Raman spectra for the coated coupon TC8 -1d and -2d cross-section.

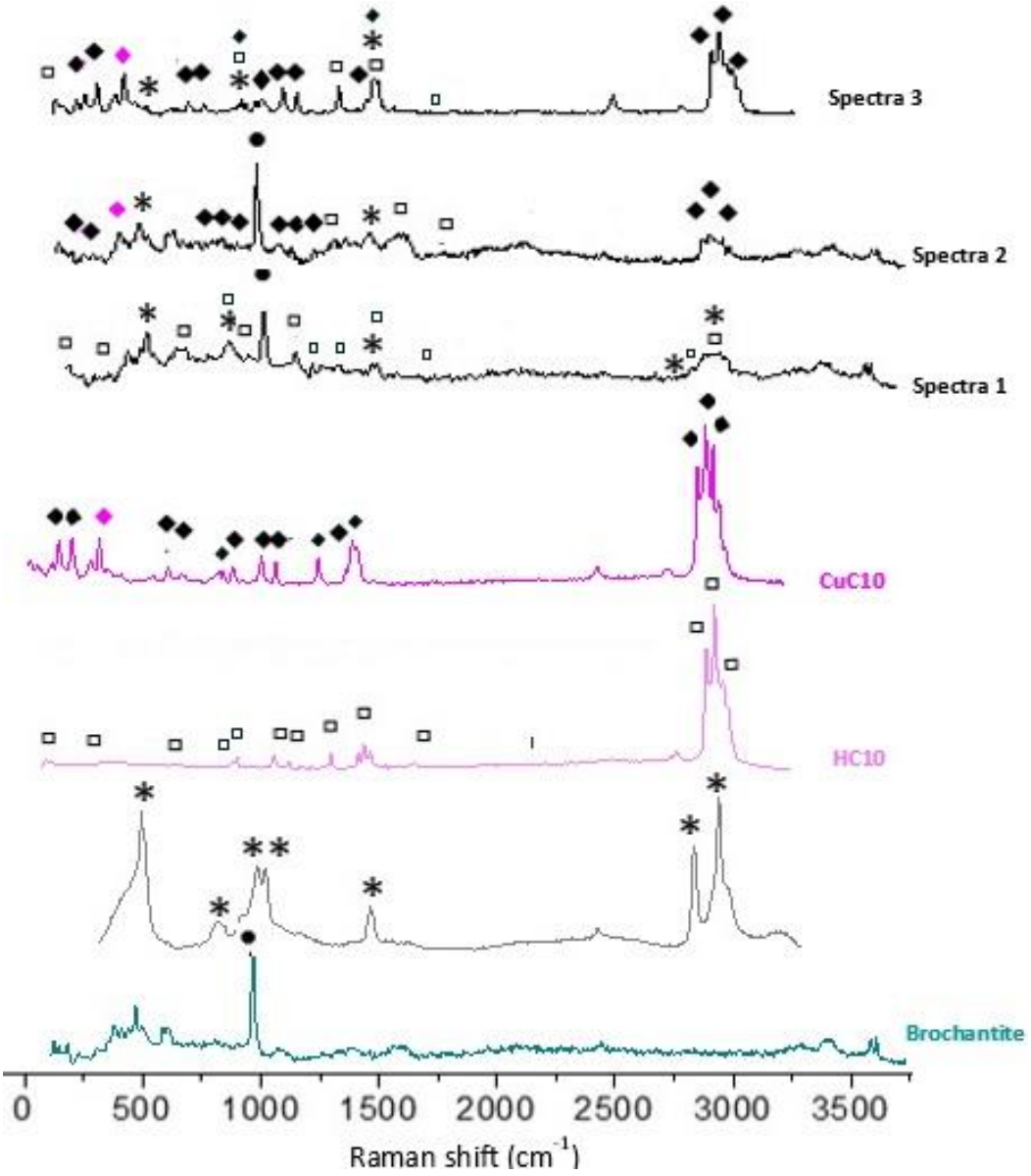

Figure 14: Z2 (spectra 1), Z3 (spectra 1 and spectra 2) and Z4 (spectra 3) characteristic Raman spectra for the coated coupon TC10 -1d and -2d cross-section.

To summarise these observations, four characteristic regions of the CL, delimitated after SEM-EDS and Raman spectroscopy characterisation, were schematically represented in Figure 15. They are representative of the undoped TMOS and TCn coated coupons, with:

- Z1 being pure cuprite – 5 µm.

- Z2 being the penetration limit zone of the xerogel doped with carboxylic acids, presenting a heterogeneous distribution of its unreacted and complexed forms: TMOS xerogel/HCn and CuCn/HCn in the brochantite layer – about 40 µm thick.

- Z3 representing the first 10 µm of the upper CL, composed mainly of xerogel and unreacted and complexed carboxylic acids, with heterogeneous areas of TMOS-based xerogel/HCn and CuCn/HCn.

- Z4 being the Si layer deposited on top of the CL and only observed for the -2d coatings. It is composed of TMOS xerogel/HCn/CuCn and its thickness can vary from 1 to 4 µm.

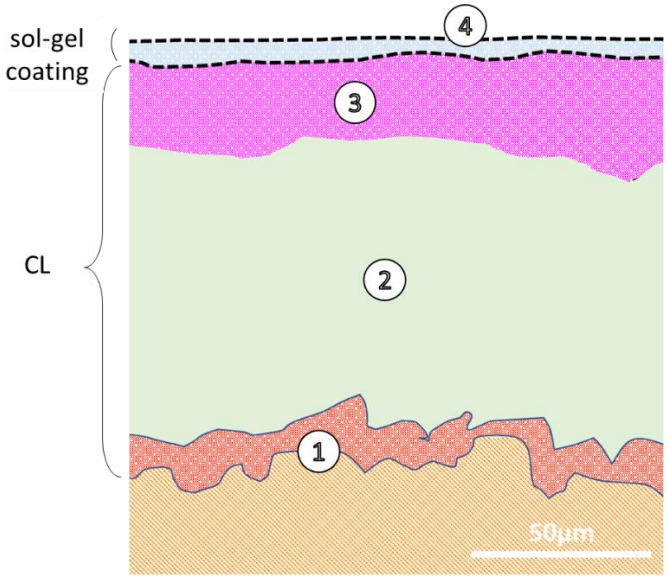

Figure 15: schematic representation of the cross section of a coupon's after TCn treatment, representative of the corrosion layer (CL) with 4 distinct regions Z1, Z2, Z3 and Z4.

Finally, to conclude this section and as a prelude to the discussion on the physico-chemical interactions happening in the CL, it is relevant to first mention the question of eco-compatibility and reversibility of the materials considered in this study for cultural heritage conservation. Yet, it is important to point out that TCn-coatings are eco-compatible. Both HCn (as such or in complexed form) and TMOS matrix are green compounds that do not damage the CL. As for their reversibility, HCn complexed in the CL can be dissolved easily with ethanol, and from an aesthetic point of view both -1d and -2d coatings have no impact on the dE* value, showing no modification of the surface, though the -2d brings an additional top layer yet transparent to the eye, while the -1d penetrated entirely in the CL. Meanwhile the TMOS xerogel, once solidified inside the porosity at the micrometric and nanometric scales, could be considered having a strengthening effect for the CL, increasing its resistance. Indeed siloxane-based xerogels have been used since a few decades now in that field of stone conservation. Studies conducted in that area demonstrated that the silica network penetrated deep into the stone porosity, polymerizing inside the pores when entering in contact with humidity present in the surrounding atmosphere and leading to the formation of a strong and stable siloxane network [73].

3.4. Mechanisms of penetration of the TCn-Sols in the CL

To explain the existence of the four regions in the CL that we observed for all TCn-coated coupons, we now propose a penetration mechanism for the TCn-Sol explaining the presence of the TMOS-based xerogel deeply inside the CL.

First, it is important to consider the evolution of the TCn-Sol itself during the hydrolysis-condensation steps of the silica precursor TMOS, prior to the coupon coating. At the beginning of the reaction the Sol consists in a mixture of TMOS, acetone, water, and carboxylic acid HCn. Acetone was chosen as co-solvent to solubilise HCn compounds and obtain a homogeneous Sol but also because of its fast evaporation during the dip-coating process. During the sol-gel process, the alkoxide groups of TMOS hydrolyse in the presence of water inducing the release of methanol (MeOH) (4 MeOH/1 TMOS for a complete hydrolysis, eq. (1)). The resulting silanol groups condense together to form the SiO_2 network with the release of water (2 H_2O/1 TMOS for a complete condensation, eq. (2), (3)).

$Si(OCH_3)_4 + H_2O \rightarrow Si(OCH_3)_3OH + CH_3OH$ eq. (1)

$Si(OCH_3)_4 + Si(OCH_3)_3OH \rightarrow \text{–SiOSi–} + CH_3OH$ eq. (2)

$Si(OCH_3)_3OH + Si(OCH_3)_3OH \rightarrow \text{–SiOSi–} + HOH$ eq. (3)

These reactions strongly depend on the pH of the Sol. The presence of HCn acids should acidify the Sol, thus accelerating the hydrolysis reaction but decelerating the condensation reaction. It is therefore important to discuss further the potential pKa evolution of HCn in a hydro-organic Sol that displays a high concentration of carboxylic acid. Despite the fact that pKa values of carboxylic acid with a chain longer than 3 in acetone-water mixtures were not previously determined in the literature, some interesting data can be found in J.P. Morel's study [74]. Indeed, the author studied the acetic and benzoic acid dissociation in various binary hydro-organic mixtures. He showed that the pKa of acetic acid can significantly increase in acetone-water and methanol-water mixtures when the proportion of the organic solvent (in weight %) increases from 10 to 90 (shifting from 4.9 to 9.6). In the present case, the Sol was a mixture of TMOS/Acetone/HCn/H2O at molar ratio 1/4/0.34/8, meaning a concentration of 0.79 g/mL for acetone and 1.00 g/mL for water. Considering the molar mass of 58.08 g/mol for acetone and 18.02 g/mol for water, the acetone-water mixture relative concentration was 61.6/38.4 wt% at the beginning of the synthesis. Based on Morel's study (Table 1 of Ref [74]) and knowing that pKa values of acetic acid and HCn acids in water are very similar for n = 7, 8 and 10 (pKa of acetic acid is 4.8; pKa of HC7 4.8; pKa of HC8 4.9; pKa of HC10 4.9) and assuming that the pKa of long chain acids would change similarly with the composition of co-

solvents the pKa of HCn acids in the Sol in such mixture would be between 6.5 and 7. At the end of hydrolysis and condensation, when gelation occurs and before evaporation of co-solvents, their concentrations can be estimated: if hydrolysis and condensation reactions were complete, water, acetone and MeOH proportions would then be 33.4/42.9/23.7 wt% (calculated with the g/mL concentration after complete reaction for eq (1), (2) and (3), and the molar mass of methanol of 32.04 g/mol). In such ternary mixture, still referring to the J.P. Morel study (Table 1 of Ref [74]), and considering the herby solvents Acetone/MeOH/H_2O with 42.9 wt% of acetone, the pKa of HCn would be around 5.5. Thus, the ionisation of HCn acids would have decreased from 6.5-7.0 to 5.5 during the hydrolysis-condensation process. Note that HCn acids have a low solubility in pure water (0.79 g/L) but they are completely soluble in acetone or MeOH and in the binary Acetone/H_2O and ternary Acetone/MeOH/H_2O mixtures. Since the pH of such hydro-organic mixture is not known, it is not possible to evaluate the proportion of deprotonated HCn molecules, which is of importance in the formation of CuCn complexes. On the contrary, once the volatile organic solvents are removed and prior to water evaporation, it is possible to evaluate the intrapore pH of the TMOS xerogel and the percentage of deprotonated HCn in the porous network.

With these considerations, we will now describe the different steps of the sol evolution during the dip-coating process. Since the dip-coating was applied 20 minutes before the gelation point, at this stage nanometric SiO_2 particles were present and the pKa of HCn molecules in the ternary mixture Acetone/MeOH/H_2O was between 6.5-7.0 and 5.5. HCn molecules were either trapped into the nanometric SiO_2 particles or remained free in the Acetone/MeOH/H_2O ternary mixture.

The first step of the coupon dip-coating process corresponded to the dipping of the coupon into the Sol, with an incomplete condensation. At this stage, a certain amount of the Sol covered the surface of the coupon and penetrated in the pores of the porous CL, filling them via a transport process driven by capillarity phenomena (Figure 16). Indeed, the CL, mostly composed of brochantite, is a highly porous material with micrometric and nanometric pore networks [52], that can be filled with a liquid solution. In Figure 16 we illustrate a schematic representation of the examined TCn coated coupon's CL in cross-section. The CL was represented with the brochantite layer in light green and the cuprite layer in brown at the interface with the metal. The pores in the brochantite were represented by heterogenous cavities filled with the Sol illustrated in light blue. The HCn molecules doping the Sol were represented by dots. Note that for clarity, brochantite's pores were represented out of scale. The analyses of the EDS profiles of the coupons cross-sections presented earlier indicated that the TCn-Sols used in this study were sufficiently fluid to penetrate deeply into the CL, up

to 60% in depth of this latter. Thus, during this first step of dip-coating, the CL was filled with the Sol containing Acetone, MeOH, H_2O, TMOS, nanometric particles of SiO_2, and HCn molecules, these latter being either trapped in the SiO_2 network or staying free in the Acetone/MeOH/H_2O ternary mixture. This was confirmed by the Raman analyses on the cross section of the CL, indicating a Z2 region composed of a mixed phase of TMOS/HCn, corresponding to the xerogel doped with carboxylic acids.

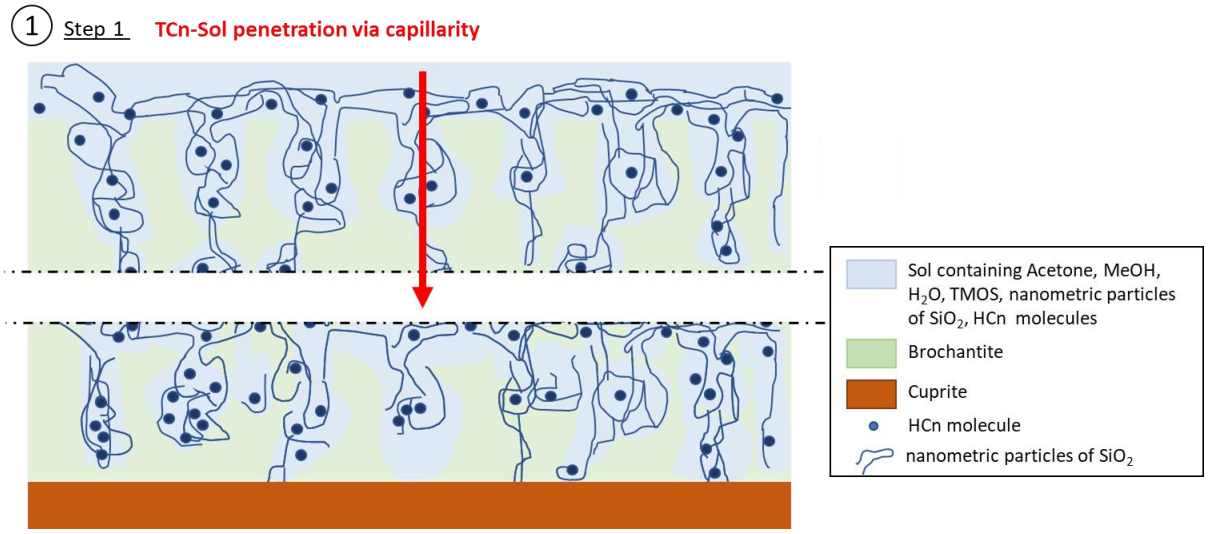

Figure 16: schematic representation TCn-Sol penetration into the CL - first step.

The second step corresponded to the concomitant condensation of the silanol groups of nanometric particles, increasing the SiO_2 porous network, in which HCn molecules were trapped, and the drying process with expulsion and evaporation of the other solvents of the Sol (Figure 17). At this point, when the coupon was withdrawn from the Sol, evaporation of the very volatile acetone occurred almost instantly. The CL contained then MeOH, H_2O, nanometric particles of SiO_2, and HCn, either trapped into this SiO_2 network or staying free in the MeOH/H_2O binary mixture. The MeOH, more volatile than water evaporated first, and since HCn molecules were poorly soluble in pure water, MeOH molecules drained the HCn molecules while migrating to the surface. This phenomenon led to the formation of a heterogeneous domain in the upper part of the CL with HCn in higher concentration (FIgure 17 step 2A). This heterogeneous domain was observed in the studied coupons, corresponding to the Z3 region described earlier in the SEM-EDS and Raman analyses and presenting a mixed TMOS xerogel/HCn phase.

At the end of the condensation and drying processes, the xerogel solidified in the CL porosities and a fraction of water and HCn molecules remained in the CL pores, either trapped in the SiO_2 network or free in the interstitial solution of the CL's pores. It is important to discuss, at this stage of the process, the HCn molecules state of protonation in presence of the remaining water. The pKa of HCn in water being around 4.8 (after JP.Morel [74]), for n=7, 8 and 10 the

proportion of protonated/deprotonated species depends on the intrapore pH of the TMOS-based xerogel. Bamogo et al. studied the intrapore pH of transparent xerogels doped with a pH-sensitive dye [75]. The xerogels were produced with Sols containing TMOS. The studies were based on the dissociation of bromothymol blue (BTB), a dye which displays a pKa of 7.1 close to that of deionized water (7.0). The protonated and deprotonated BTB displaying distinctive absorption bands, by measuring optically the proportions of BTB acidic and basic forms in the pores filled with water, the authors deduced an intrapore pH of 4.65 for TMOS-based xerogel. They explained the low intrapore pH of TMOS in terms of the presence of free acidic Si-OH groups that did not condense and deprotonated in the pores filled with water molecules. By applying the intrapore pH of 4.65 determined by Bamogo for our TMOS-based xerogel doped with HCn, and taking into account that the HCn pKa in water is around 4.8, one can deduce that the proportions of protonated HCn and deprotonated HCn should be close to 50%, based on the following equation (4):

$$Log\left(\frac{anion}{acid}\right) = pH\ (water) - pKa\ \ i.e,\ \frac{anion}{acid} = 10^{(pH-pKa)} \quad \text{eq. (4)}$$

Thus, the Z2 and Z3 regions of our coupon's CL would contain HCn molecules present under their protonated and deprotonated form at 50% (Figure 17 step 2B).

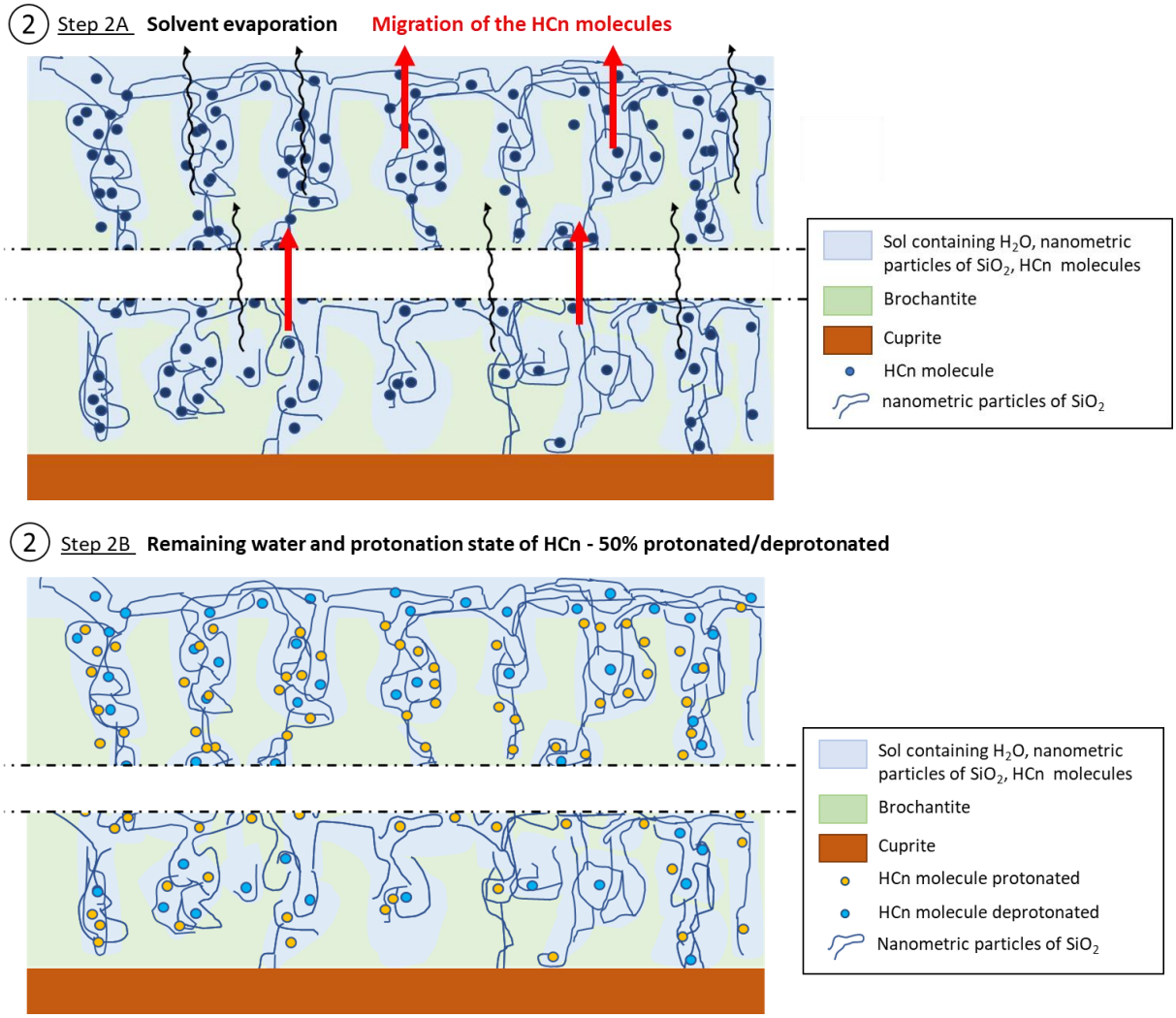

Figure 17: schematic representation of the TCn-Sol penetration into the CL - step 2 A and B.

In addition, to fully examine the interaction between the brochantite and HCn molecules in the CL, it is important to consider the behaviour of the brochantite in the vicinity of the xerogel. The xerogel intrapore pH of 4.65 and the proportion of deprotonated HCn provide an acidic environment for the brochantite. Referring to the brochantite behaviour relative to its pH environment, we drew a thermodynamic diagram, to evaluate its stability domain. Figure 18 presents the evolution of Cu^{2+} concentration depending on the pH in an aerated sulphate solution.

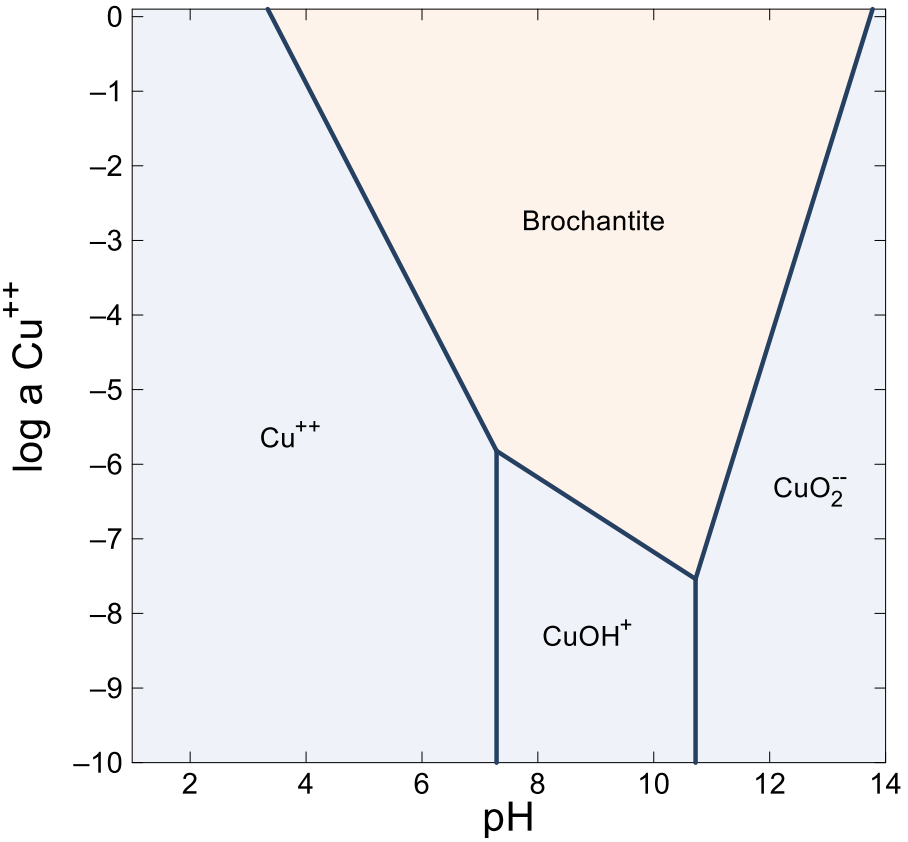

Figure 18: thermodynamic diagram representing the evolution of log Cu^{2+} against the pH, with $[SO_4^{2-}]$ set to 1.10^{-5} mol/L, $[H_2O]$ to 1 mol/L and a redox potential (Eh) set to 1 volt – Temperature is 25°C and Pressure is 1,013 bars.

It shows that brochantite is the most stable for pH values between 7 and 11 and for a low concentration of Cu^{2+} ions. The diagram also indicates that at lower pH, such as those supposedly present in the brochantite pores at the final stage of the drying process (pH = 4.6-4.8), the brochantite tends to dissolve with the formation of Cu^{2+} ions. The reaction of Cu^{2+} ions with deprotonated HCn molecules in the vicinity will be favoured leading to the formation of copper carboxylate compounds (CuCn) (Figure 19) as shown below (eq. (5)):

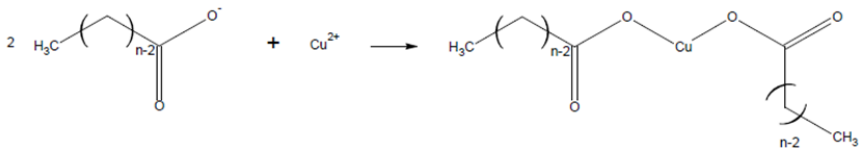

eq. (5)

Such mechanism is supported by the results obtained with the Raman spectroscopy as exposed above, showing Z2 and Z3 regions composed of a mixed phase of HCn/CuCn.

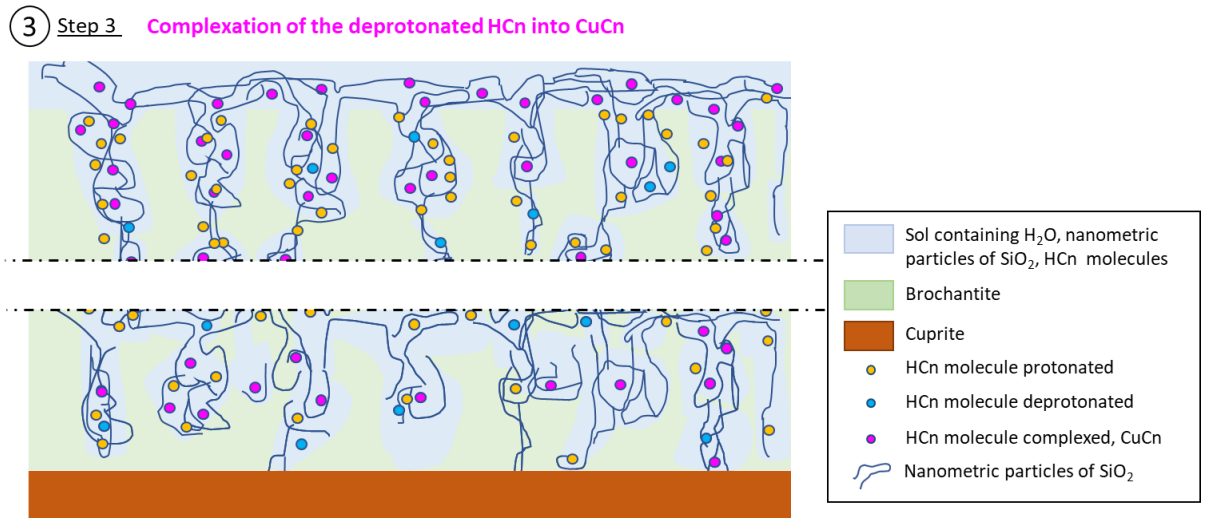

Figure 19: schematic representation of the TCn-Sol penetration into the CL - step 3.

Because of the complexation of the Cu^{2+} with the HCn, the Cu^{2+} should decrease in the brochantite pores and the local pH should increase slightly because the HCn is converted into CuCn. But it is also necessary to take into account the release of H^+ ions from the SiO-H condensation and the HCn ionisation that happens simultaneously in the xerogel. This could decrease locally the pH inside the pores and maintain a higher dissolution rate of brochantite. Meanwhile, another aspect to consider with brochantite dissolution is the release of SO_4^{2-} and OH^- ions into the pores. Therefore, considering this final stage of the gel drying process, the pH should be between 4.6 and 4.8 because of the presence of HCn and the SiO_2 network, but it should increase with the release of SO_4^{2-} and OH^- ions Thus, we present a thermodynamic diagram displaying the evolution of the SO_4^{2-} concentration versus the pH environment, drawn in Figure 20. This diagram shows that for a SO_4^{2-} concentration increases, and considering a pH of 4.6-4.8, the brochantite becomes more stable. The CL would then reach a stabilisation point where the brochantite would remain stable and stop dissolving, while containing a certain amount of HCn not complexed with the released Cu^{2+}. This was confirmed by the micrometric observations conducted on cross- sections of the examined coupons, which showed no further increase of the porosity network of the CL after treatment.

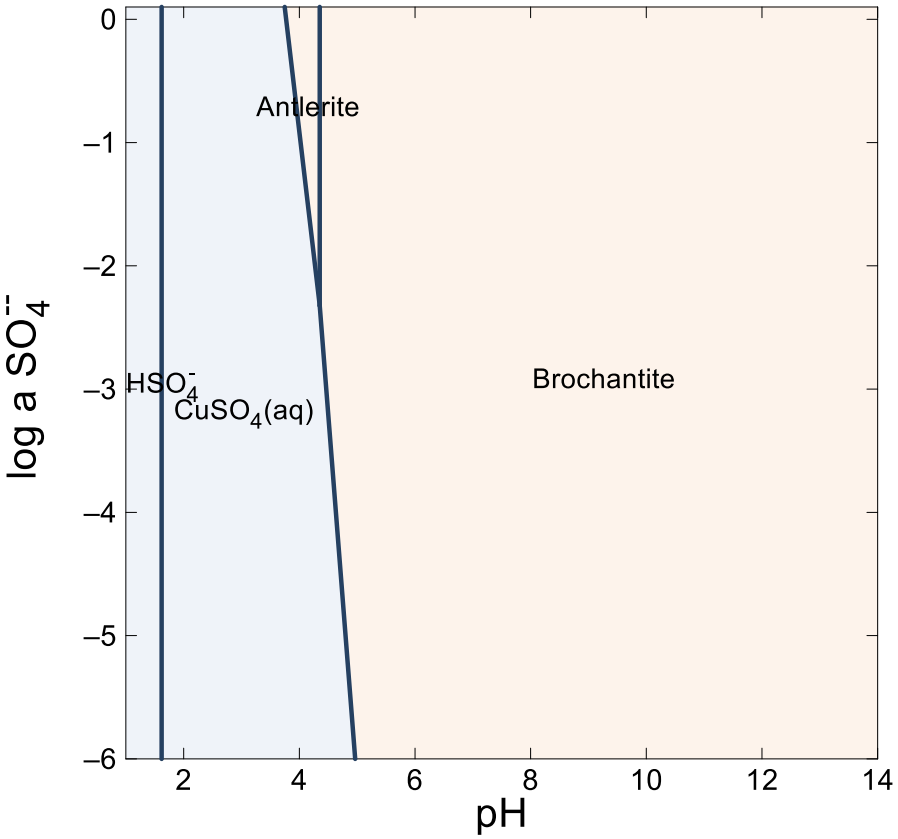

Figure 20: thermodynamic diagram representing the evolution of log SO_4^{2-} against the pH, with $[Cu^{2+}]$ set to 1.10^{-2} mol/L, $[H_2O]$ to 1 mol/L and a redox (Eh) set to 1 volt – Temperature is 25°C and Pressure is 1.013 bars.

Our last consideration concerned the possible reservoir effect of the remaining HCn molecules in the artefact's CL while exposed to atmospheric environment. For such artefacts as presented in this study, this means considering the surrounding atmospheric conditions, especially rains and relative humidity (RH) that can vary in so-called wet-dry cycles. With reference to the contact angle measurements exposed above, we demonstrated that TCn coatings led to hydrophobic surfaces for the copper coupons, by forming copper carboxylates that covered the CL. These results implied that there should be a limited liquid-water penetration into the CL. However, the hydrophobic surface does not prevent from a vapour water exchange between the atmosphere and the CL [52],[76]. Thus, if we examine humid conditions for the coupons, the CL should remain in equilibrium with the water in the atmosphere, implying water presence in the CL's pores. In the CL, the HCn molecules either trapped into the SiO_2 network or free in the remaining H_2O, would then remain at 50% protonated and deprotonated. Meanwhile if we examine dryer conditions, the water should evaporate partially from the CL, decreasing drastically the water content in the CL's pores. This water evaporation would correspond to a deionization of the HCn molecules. In this case, we could consider that the neutral HCn molecules would form a reservoir of unreacted HCn in the CL. Therefore, depending on the RH environment of the CL, there could be water exchange

between the CL and the atmosphere, leading to a change of the ionization state of the HCn molecules and as well to the formation of CuCn in the CL.

4. Conclusion

The results of this work have shown that the tetramethyl orthosilicate-based sol-gel coatings doped with carboxylic acid compounds, the TCn coatings, can bring an effective protection for ancient copper substrates via two different principles. A first protection was obtained with the formation of copper carboxylate complexes at the surface of the corroded copper, providing a water-repellent surface for the ancient metal. The high hydrophobicity of the surface was evaluated via contact angles as high as 120° to 150°. The second protection was provided by the deep penetration of TCn into the copper corrosion layer, forming a reservoir of carboxylic acids, effective corrosion inhibitors. With a very detailed study of the composition of the TCn-coated sample cross-sections, in relation with the tetramethyl orthosilicate-based xerogel and carboxylic acids properties (pH, pKa in hydro-organic media), we could give a complete scheme of the penetration of TCn into the corrosion layer and assess the nature of the reactions involving the brochantite and the acids in the vicinity of the xerogel. Indeed, interstitial water brought by water vapour from atmosphere played a crucial role in regulating the xerogel intrapore pH and the dissolution of brochantite in acidic environment. Through TCn, corrosion could be stopped by the formation of copper carboxylate complexes into the ancient copper corrosion layer. On the other hand, in dry conditions, when interstitial water had evaporated, the xerogel provided a reservoir of neutral unreacted carboxylic acids, enabling a long-term protection to the coated artefacts.

Colorimetric results however indicated that the carboxylic acid alkyl chain influenced the surface colour of the TCn-coated samples, with a variation of colour at the strongest when using decanoic acid as doping agent. Because of this aesthetic criterion and based on the physic-chemical characterisation obtained, we can propose octanoic acid as best doping agent to fulfil all hydrophobic properties, colorimetric requirements, and deep acid penetration and reaction in the corrosion layer to possibly inhibit corrosion.

In addition to the reversibility of TCn-coatings on old copper CL, it is important to point out that both carboxylic acid and TMOS are eco-compatible and do not damage the CL. The complexed HCn present in the CL can be dissolved with ethanol. The coating in itself has slight to no (for the 1d-coating) aesthetic impact on the old copper surface since it is not deposited on it but only penetrates in the pores of the CL. Considering this last property, it can be questioned whether the TMOS-based xerogel can be considered as a CL strengthening component. These properties have to be studied in more depth.

Further experiments are planned to study long term exposure of TCn coatings to outdoor environments in order to assess long term corrosion protection. These studies will be carried out over a full year by exposing a series of coated copper samples to the outdoor atmosphere and performing hydrophobicity and chemical composition analyses of cross-sections every three months. Another more rapid method would involve exposing samples to simulated extreme atmospheric conditions by alternating exposure to heavy rain, high heat and low temperatures to accelerate corrosion conditions.

In addition, a next step towards industrial applications will be the up-scale study of TCn coatings on coper-based alloys. Particular attention will be paid to the stability of TCn over long storage period, with the possibility of activating the condensation process before a programmed coating time. Spray-coating will be examined as well as the study of spray conditions for coating complex artefacts or large surfaces such as copper roofs.

CRediT authorship contribution statement

Silvia Lob: Conceptualization, Methodology, Investigation, Writing – original draft, Writing – review & editing. Delphine Neff: Conceptualization, Funding acquisition, Supervision, Writing – review & editing. Thu-hoa Tran-thi: Conceptualization, Supervision, Writing – review & editing. Christine Richter: Supervision – review & editing. Charles Rivron: Investigation.

Declaration of competing interest

The authors declare that they have no known competing financial interests or personal relationships that could have appeared to influence the work reported in this paper.

Data availability

Data will be made available on request.

Acknowledgments

This research was funded by the *Fondation des Sciences du Patrimoine*. We thank Aurélia Azéma for her help settling the PhD objectives and the LRMH for supplying the ancient copper plates from the Saint Matin Church (Metz, France). We also thank A-Corros for the follow-up on the project, providing interesting insights on the materials developed and allowing us to test the sol-gel doped-coating using application methods specific to the conservation of metallic heritage.

References

[1] D. Wang, G.P. Bierwagen, Sol-gel coatings on metals for corrosion protection, Prog. Org. Coatings. 64 (2009) 327–338. https://doi.org/10.1016/j.porgcoat.2008.08.010.

[2] M.L. Zheludkevich, R. Serra, M.F. Montemor, K.A. Yasakau, I.M.M. Salvado, M.G.S. Ferreira, Nanostructured sol-gel coatings doped with cerium nitrate as pre-treatments for AA2024-T3 Corrosion protection performance, Electrochim. Acta. 51 (2005) 208–217. https://doi.org/10.1016/j.electacta.2005.04.021.

[3] R.B. Figueira, Hybrid sol-gel coatings for corrosion mitigation: A critical review, Polymers (Basel). 12 (2020) 9–12. https://doi.org/10.3390/polym12030689.

[4] J. Zarzycki, Past and Present of Sol-Gel Science and Technology, J. Sol-Gel Sci. Technol. 8 (1997) 17–22. https://doi.org/10.1007/BF02436811.

[5] M.M.F. Choi, Progress in enzyme-based biosensors using optical transducers, Microchim. Acta. 148 (2004) 107–132. https://doi.org/10.1007/s00604-004-0273-8.

[6] P.C.A. Jerónimo, A.N. Araújo, M. Conceição, Optical sensors and biosensors based on sol-gel films, Talanta. 72 (2007) 13–27. https://doi.org/10.1016/j.talanta.2006.09.029.

[7] M.R.N. Monton, E.M. Forsberg, J.D. Brennan, Tailoring sol-gel-derived silica materials for optical biosensing, Chem. Mater. 24 (2012) 796–811. https://doi.org/10.1021/cm202798e.

[8] Y. Wang, S. Tu, A.N. Pinchuk, M.P. Xiong, Active drug encapsulation and release kinetics from hydrogel-in-liposome nanoparticles, J. Colloid Interface Sci. 406 (2013) 247–255. https://doi.org/10.1016/j.jcis.2013.05.081.

[9] H. Cho, J. Gao, G.S. Kwon, PEG-b-PLA micelles and PLGA-b-PEG-b-PLGA sol–gels for drug delivery, J. Control. Release. 240 (2016) 191–201. https://doi.org/10.1016/j.jconrel.2015.12.015.

[10] H.Y. Lee, H.E. Kim, S.H. Jeong, One-pot synthesis of silane-modified hyaluronic acid hydrogels for effective antibacterial drug delivery via sol–gel stabilization, Colloids Surfaces B Biointerfaces. 174 (2019) 308–315. https://doi.org/10.1016/j.colsurfb.2018.11.034.

[11] V.J. Hernández-Abad, E.G. Sánchez-González, C. Espinosa-Contreras, R. Marroquín-Segura, J.L.A. Mora-Guevara, Y. Flores-Cabrera, Controlled release of glibenclamide from monolithic silica subdermal implants produced by the sol-gel process and its use for hyperglycaemia treatment in a murine model, Mater. Sci. Eng. C. 94 (2019) 1009–1019. https://doi.org/10.1016/j.msec.2018.10.050.

[12] C. Sanchez, L. Rozes, F. Ribot, C. Laberty-Robert, D. Grosso, C. Sassoye, C. Boissiere, L. Nicole, “Chimie douce”: A land of opportunities for the designed construction of functional inorganic and hybrid organic-inorganic nanomaterials, Comptes Rendus Chim. 13 (2010) 3–39. https://doi.org/10.1016/j.crci.2009.06.001.

[13] J.C.B. Alcázar, R.M.J. Lemos, M.C.M. Conde, L.A. Chisini, M.M.S. Salas, B.S. Noremberg, F.V. da Motta, F.F. Demarco, S.B.C. Tarquinio, N.L.V. Carreño, Preparation, characterization, and biocompatibility of different metal oxide/PEG-based hybrid coating synthesized by sol–gel dip coating method for surface modification of titanium, Prog. Org. Coatings. 130 (2019) 206–213. https://doi.org/10.1016/j.porgcoat.2019.02.007.

[14] V. Palanivel, Y. Huang, W.J. Van Ooij, Effects of addition of corrosion inhibitors to silane films on the performance of AA2024-T3 in a 0.5 M NaCl solution, Prog. Org. Coatings. 53 (2005) 153–168. https://doi.org/10.1016/j.porgcoat.2003.07.008.

[15] V. Palanivel, D. Zhu, W.J. Van Ooij, Nanoparticle-filled silane films as chromate replacements for aluminum alloys, Prog. Org. Coatings. 47 (2003) 384–392. https://doi.org/10.1016/j.porgcoat.2003.08.015.

[16] T. Sugama, Cerium acetate-modified aminopropylsilane triol: A precursor of corrosion-preventing coating for aluminum-finned condensers, J. Coatings Technol. Res. 2 (2005) 649–659. https://doi.org/10.1007/BF02774594.

[17] H. Wang, R. Akid, Encapsulated cerium nitrate inhibitors to provide high-performance anti-corrosion sol-gel coatings on mild steel, Corros. Sci. 50 (2008) 1142–1148. https://doi.org/10.1016/j.corsci.2007.11.019.

[18] K.P. Fitzgerald, J. Nairn, A. Atrens, The chemistry of copper patination, Corros. Sci. 40 (1998) 2029–2050. https://doi.org/10.1016/S0010-938X(98)00093-6.

[19] D. De Fuente, J. Simancas, M. Morcillo, Morphological study of 16-year patinas formed on copper in a wide range of atmospheric exposures, 50 (2008) 268–285. https://doi.org/10.1016/j.corsci.2007.05.030.

[20] E. Apchain, D. Neff, A. Texier, A. Azéma, F. Mirambet, D. Robcis, J.P. Gallien, A. Noumowé, P. Dillmann, Protection of bronze statuary, comparison of classical treatments and approaches with carboxylates, Eur. Corros. Congr. EUROCORR 2015. 3 (2015) 1588–1589.

[21] F. Zucchi, 24 - Sol-gel coatings for the preservation of metallic heritage artefacts, in: P. Dillmann, D. Watkinson, E. Angelini, A.B.T.-C. and C. of C.H.M.A. Adriaens (Eds.), Eur. Fed. Corros. Ser., Woodhead Publishing, 2013: pp. 540–551. https://doi.org/https://doi.org/10.1533/9781782421573.5.540.

[22] E. Cano, D. Lafuente, Corrosion inhibitors for the preservation of metallic heritage artefacts, in:

P. Dillmann, D. Watkinson, E. Angelini, A.B.T.-C. and C. of C.H.M.A. Adriaens (Eds.), Eur. Fed. Corros. Ser., Woodhead Publishing, 2013: pp. 570–594. https://doi.org/https://doi.org/10.1533/9781782421573.5.570.

[23] E. Joseph, P. Letardi, R. Mazzeo, S. Prati, M. Vandini, Innovative treatments for the potection of outdoor bronze monuments, in Proceedings of the Interim Meeting of the ICOM-CC Metal WG : Amsterdam, Netherland, 2007, Vol.5, 71–77.

[24] A. Balbo, C. Chiavari, C. Martini, C. Monticelli, Effectiveness of corrosion inhibitor films for the conservation of bronzes and gilded bronzes, Corros. Sci. 59 (2012) 204–212. https://doi.org/10.1016/j.corsci.2012.03.003.

[25] C. Chiavari, A. Balbo, E. Bernardi, C. Martini, F. Zanotto, I. Vassura, M.C. Bignozzi, C. Monticelli, Organosilane coatings applied on bronze: Influence of UV radiation and thermal cycles on the protectiveness, Prog. Org. Coatings. 82 (2015) 91–100. https://doi.org/10.1016/j.porgcoat.2015.01.017.

[26] G. Masi, A. Balbo, J. Esvan, C. Monticelli, J. Avila, L. Robbiola, E. Bernardi, M.C. Bignozzi, M.C. Asensio, C. Martini, X-ray Photoelectron Spectroscopy as a tool to investigate silane-based coatings for the protection of outdoor bronze: The role of alloying elements, Appl. Surf. Sci. 433 (2018) 468–479.

[27] G. Masi, C. Josse, J. Esvan, C. Chiavari, E. Bernardi, C. Martini, M.C. Bignozzi, C. Monticelli, F. Zanotto, A. Balbo, E. Svara Fabjan, T. Kosec, L. Robbiola, Evaluation of the protectiveness of an organosilane coating on patinated Cu-Si-Mn bronze for contemporary art, Prog. Org. Coatings. 127 (2019) 286–299. https://doi.org/10.1016/j.porgcoat.2018.11.027.

[28] E. Kiele, J. Senvaitiene, A. Griguceviciene, R. Ramanauskas, R. Raudonis, A. Kareiva, Application of sol-gel method for the conservation of copper alloys, Microchem. J. 124 (2016) 623–628. https://doi.org/10.1016/j.microc.2015.10.003.

[29] E. Rocca, C. Rapin, F. Mirambet, Inhibition treatment of the corrosion of lead artefacts in atmospheric conditions and by acetic acid vapour: Use of sodium decanoate, Corros. Sci. 46 (2004) 653–665.

[30] E. Rocca, J. Steinmetz, Inhibition of lead corrosion with saturated linear aliphatic chain monocarboxylates of sodium, Corros. Sci. 43 (2001) 891–902.

[31] Hollner, SH. (2009). Developpement de nouveaux traitements de protection a base d'acide carboxylique pour la conservation d'objets en fer du patrimoine culturel [Ph.D. thesis, Henri-Poincaré Nancy I University]. Université de Lorraine. http://docnum.univ-lorraine.fr/public/SCD_T_2009_0062_HOLLNER.pdf.

[32] S. Hollner, F. Mirambet, E. Rocca, S. Reguer, Evaluation of new non-toxic corrosion inhibitors for conservation of iron artefacts, Corros. Eng. Sci. Technol. 45 (2010) 362–366.

[33] S. Hollner, F. Mirambet, A.Texier, E. Rocca, J. Steinmetz, L. De Chimie, M. Université, H. Poincaré, Development of new non-toxic corrosion inhibitors for cultural property made of iron and copper alloys, in Proceedings of the International Conference on Conservation Strategies for Saving Indoor Metallic Collections: Cairo, Egypt, 25 Febr. – 1 March 2007, pp.156–161.

[34] Faiz, HF. (2012). Étude du mécanisme de corrosion atmosphérique à long terme des aciers: nouvelles stratégies de protection des aciers du patrimoine culturel [Ph.D. thesis, Henri-Poincaré Nancy I University]. Université de Lorraine. http://docnum.univ-lorraine.fr/public/DDOC_T_2012_0314_FAIZ.pdf.

[35] J. Peultier, E. Rocca, J. Steinmetz, Zinc carboxylating: a new conversion treatment of zinc, Corros. Sci. 45 (2003) 1703–1716.

[36] E. Rocca, F. Mirambet, P. Dillmann, M. Folzan, S. Reguer, Traitements de protection à base de dérivés d'huiles végétales pour les objets ferreux corrodés : cas de couches épaisses de « rouille », in: Proceedings of the Conference on Science des Matériaux du Patrimoine Culturel: Paris, France, Nov. 2012, pp. 120–125.

[37] C. Rapin, P. Steinmetz, J. Steinmetz, Temporary protection of metals against atmospheric corrosion by saturated straight chain aliphatic monocarboxylates. Mechanisms of inhibition, NACE International, Houston, TX (United States), 1998.

[38] C. Rapin, P. Steinmetz, J. Steinmetz, Etude de l'inhibition de la corrosion aqueuse du cuivre par les carboxylates linéaires saturés. I. Pouvoir inhibiteur des carboxylates linéaires de formule CH3 (CH2) n-2COONa, Rev. Métallurgie. 93 (1996) 281–290.

[39] G.T. Hefter, N.A. North, S.H. Tan, Organic corrosion inhibitors in neutral solutions; part 1—inhibition of steel, copper, and aluminum by straight chain carboxylates, Corrosion. 53 (1997)

657–667.

[40] V. Beucler-Bour, Etude d'une famille d'inhibiteurs organiques de la corrosion de l'acier, (1993).

[41] E. Rocca, G. Bertrand, C. Rapin, J.C. Labrune, Inhibition of copper aqueous corrosion by non-toxic linear sodium heptanoate: mechanism and ECAFM study, J. Electroanal. Chem. 503 (2001) 133–140.

[42] E. Rocca, C. Rapin, F. Mirambet, Inhibition treatment of the corrosion of lead artefacts in atmospheric conditions and by acetic acid vapour: Use of sodium decanoate, Corros. Sci. 46 (2004) 653–665.

[43] C. Chiavari, C. Martini, G. Poli, D. Prandstraller, Conservation of organ pipes: protective treatments of lead exposed to acetic acid vapours, in: Met. 04. Proc. Int. Conf. Met. Conserv. Natl. Museum Aust. Canberra, 2004: pp. 281–293.

[44] Milbled, SM. (2010). La stabilisation de la corrosion réactivée des alliages cuivreux : étude comparative du décanoate de sodium et du benzotriaole [Ph.D. thesis Paris 1 University PanthéonSorbonne].Academia.https://www.academia.edu/20780985/La_stabilisation_de_la_corrosion_r%C3%A9activ%C3%A9e_des_alliages_cuivreux_%C3%A9tude_comparative_du_d%C3%A9canoate_de_sodium_et_du_benzotriazole.

[45] E. Ferrari, D. Neff, E. Apchain, M. Bayle, P. de Viviés, J.-B. Memet, P. Dillmann, Assessing the Interaction between Corrosion Inhibitors and the Historical Corrosion Layer on Copper Claddings Based on Global and Micrometric-Scale Analysis, in: Proceedings of the Interim Meeting of ICOM-CC Metal Conference: Neuchatel, Switzerland, 2-6 Sept. 2019.

[46] M. Donnici, M.A. Baldo, S. Daniele, An electrochemical study on the interaction between copper ions and the eco-friendly corrosion inhibitor decanoic acid in a 50% (v/v) ethanol/water mixture, J. Mol. Liq. 332 (2021) 115829. https://doi.org/10.1016/j.molliq.2021.115829.

[47] Z. Wang, J. Li, H. Zhang, Micron scale and nanoscale structure of mesoporous silica thin films, J. Non. Cryst. Solids. 354 (2008) 3072–3077. https://doi.org/10.1016/j.jnoncrysol.2008.01.027.

[48] C. Sanchez, G.J. Galo, F. Ribot, D. Grosso, Design of functional nano-structured materials through the use of controlled hybrid organic-inorganic interfaces, Comptes Rendus Chim. 6 (2003) 1131–1151. https://doi.org/10.1016/j.crci.2003.06.001.

[49] E. Voltz, De quelques aspects de la cathédrale de Metz, in Mémoires de l'Académie nationale de Metz, France, 1986, p.65-88.

[50] M. Morcillo, T. Chang, B. Chico, D. de la Fuente, I. Odnevall Wallinder, J.A. Jiménez, C. Leygraf, Characterisation of a centuries-old patinated copper roof tile from Queen Anne's Summer Palace in Prague, Mater. Charact. 133 (2017) 146–155. https://doi.org/10.1016/j.matchar.2017.09.034.

[51] T. Chang, A. Maltseva, P. Volovitch, I. Odnevall Wallinder, C. Leygraf, A mechanistic study of stratified patina evolution on Sn-bronze in chloride-rich atmospheres, Corros. Sci. 166 (2020) 108477. https://doi.org/10.1016/j.corsci.2020.108477.

[52] Apchain, EA. (2018). Apport des traitements carboxylates à la protection des alliages cuivreux [Ph.D. thesis, Cergy-Pontoise University]. HAL. https://hal.science/tel-01850272.

[53] E. Apchain, D. Neff, J.-P. Gallien, N. Nuns, P. Berger, A. Noumowé, P. Dillmann, Efficiency and durability of protective treatments on cultural heritage copper corrosion layers, Corros. Sci. (2021) 109319. https://doi.org/https://doi.org/10.1016/j.corsci.2021.109319.

[54] A. Krätschmer, I. Odnevall Wallinder, C. Leygraf, The evolution of outdoor copper patina, Corros. Sci. 44 (2002) 425–450. https://doi.org/10.1016/S0010-938X(01)00081-6.

[55] Santoro, CS. (2011). Caractérisation de composés hybrides organique-inorganique à base de cuivre rencontrés en peinture : étude de leur formation et transformation [Ph.D. thesis, Cergy-Pontoise University]. HAL. https://theses.hal.science/tel-00938219.

[56] A.V. Rao, M.M. Kulkarni, Hydrophobic properties of TMOS/TMES-based silica aerogels, Mater. Res. Bull. 37 (2002) 1667–1677. https://doi.org/10.1016/S0025-5408(02)00795-X.

[57] R.L. Frost, Raman spectroscopy of selected copper minerals of significance in corrosion, Spectrochim. Acta. 59 (2003) 1195–1204. file://drec-ca-001071/commun archeo/bibliographie/Articles pdf/Spectro Chim Acta_Frost_2003.pdf.

[58] W. Martens, R.L. Frost, J.T. Kloprogge, P.A. Williams, Raman spectroscopic study of the basic copper sulphates - Implications for copper corrosion and "bronze disease," J. Raman Spectrosc. 34 (2003) 145–151. https://doi.org/10.1002/jrs.969.

[59] Z. Sassi, J.C. Bureau, A. Bakkali, Spectroscopic study of TMOS-TMSM-MMA gels: Previously identification of the networks inside the hybrid material, Vib. Spectrosc. 28 (2002) 299–318. https://doi.org/10.1016/S0924-2031(02)00009-7.

[60] Robinet, LR. (2006). The role of organic pollutants in the alteration of historical soda silicate glasses [Ph.D. thesis, University of Edinburg and Pierre et Marie Curie Paris VI University]. HAL. https://theses.hal.science/tel-00088408.

[61] F. Génin, F. Quilès, A. Burneau, Infrared and Raman spectroscopic study of carboxylic acids in heavy water, Phys. Chem. Chem. Phys. 3 (2001) 932–942. https://doi.org/10.1039/b008897h.

[62] A. Doyle, J. Felcman, M.T. do P. Gambardella, C.N. Verani, M.L.B. Tristão, Anhydrous copper(II) hexanoate from cuprous and cupric oxides. The crystal and molecular structure of Cu2(O2CC5H11)4, Polyhedron. 19 (2000) 2621–2627. https://doi.org/10.1016/S0277-5387(00)00568-4.

[63] D.C. Pereira, D.L.A. De Faria, V.R.L. Constantino, CuII hydroxy salts: Characterization of layered compounds by vibrational spectroscopy, J. Braz. Chem. Soc. 17 (2006) 1651–1657. https://doi.org/10.1590/S0103-50532006000800024.

[64] E. Franceschi, P. Letardi, G. Luciano, Colour measurements on patinas and coating system for outdoor bronze monuments, J. Cult. Herit. 7 (2006) 166–170.

[65] L. Gianni, M. Adriaens, M. Cavalini, S. Natali, V. Volpe, L. Zortea, Reflectance curves and CIE L* a* b* parameters to describe patina characteristics and corrosion mechanism on bronze alloys, Cult. E Sci. Del Color. (2014) 38–43.

[66] S. Lob, Développement de traitements innovants à base de sol-gels dopés en acides carboxyliques pour la protection du patrimoine cuivreux : compréhension des mécanismes de pénétration dans la couche de produits de corrosion par une approche multi-échelle, CY Cergy paris University, n.d.

[67] S.V.S. Prasad, I. institute of technology V. Sitakara Rao*, Department of chemistry, I. Kharagpur, Thermal analysis, X-ray diffraction and Infrared spectroscopic study of synthetic brochantite, 30 (1984) 603–609.

[68] N. Koga, J.M. Criado, H. Tanaka, Reaction pathway and kinetics of the thermal decomposition of sunthetic brochantite, J. Therm. Anal. 49 (1997) 1467–1475.

[69] W. Fiddler, W.E. Parker, A.E. Wasserman, R.C. Doerr, Thermal Decomposition of Ferulic Acid, J. Agric. Food Chem. 15 (1967) 757–761. https://doi.org/10.1021/jf60153a003.

[70] M. Criado, I. Sobrados, J. Sanz, Polymerization of hybrid organic-inorganic materials from several silicon compounds followed by TGA/DTA, FTIR and NMR techniques, Prog. Org. Coatings. 77 (2014) 880–891. https://doi.org/10.1016/j.porgcoat.2014.01.019.

[71] Lob, SL. (2021). Développement de traitements innovants à base de sol-gels dopes en acides carboxyliques pour la protection du patrimoine cuivreux : compréhension des mécanismes de pénétration dans la couche de produits de corrosion par une approche multi-échelle [Ph.D. thesis, CY Cergy Paris University]. HAL. https://theses.hal.science/tel-03655051.

[72] T.E. Graedel, Copper patinas formed in the atmosphere--I. introduction, Corros. Sci. 27 (1987) 639–657.

[73] M.J. Mosquera, D.M. De Los Santos, A. Montes, L. Valdez-Castro, New nanomaterials for consolidating stone, Langmuir. 24 (2008) 2772–2778. https://doi.org/10.1021/la703652y.

[74] J.P. Morel, Dissociation relative de acides acétique et benzoïque en milieux hydroorganiques**,** Proceedings in Science Pour l'Ingénieur n°127, France, Nov. 1969.

[75] Bamogo, WB. (2015). Capteurs chimiques à base de matrices nanoporeuses pour la détection de métabolites volatils de la tuberculose [Ph.D. thesis, Paris Sud University]. HAL. https://tel.archives-ouvertes.fr/tel-01128414.

[76] Mchirgui, WM. (2013). Modélisation des transferts hydriques dans les milieux poreux partiellement saturés par homogénéisation périodique : Application aux matériaux cimentaires [Ph.D. thesis, La Rochelle University]. HAL. https://theses.hal.science/tel-00823902.

Appendices

Appendix A

The SEM electronic images obtained from the TCn coated coupons surfaces presented in Fig.3 showed that the external CL was covered with flower-shaped compounds. They were later identified as copper carboxylates (CuCn) by Raman analyses as presented in this appendix A, Fig.A.1, Fig.A.2 and Fig.A.3.

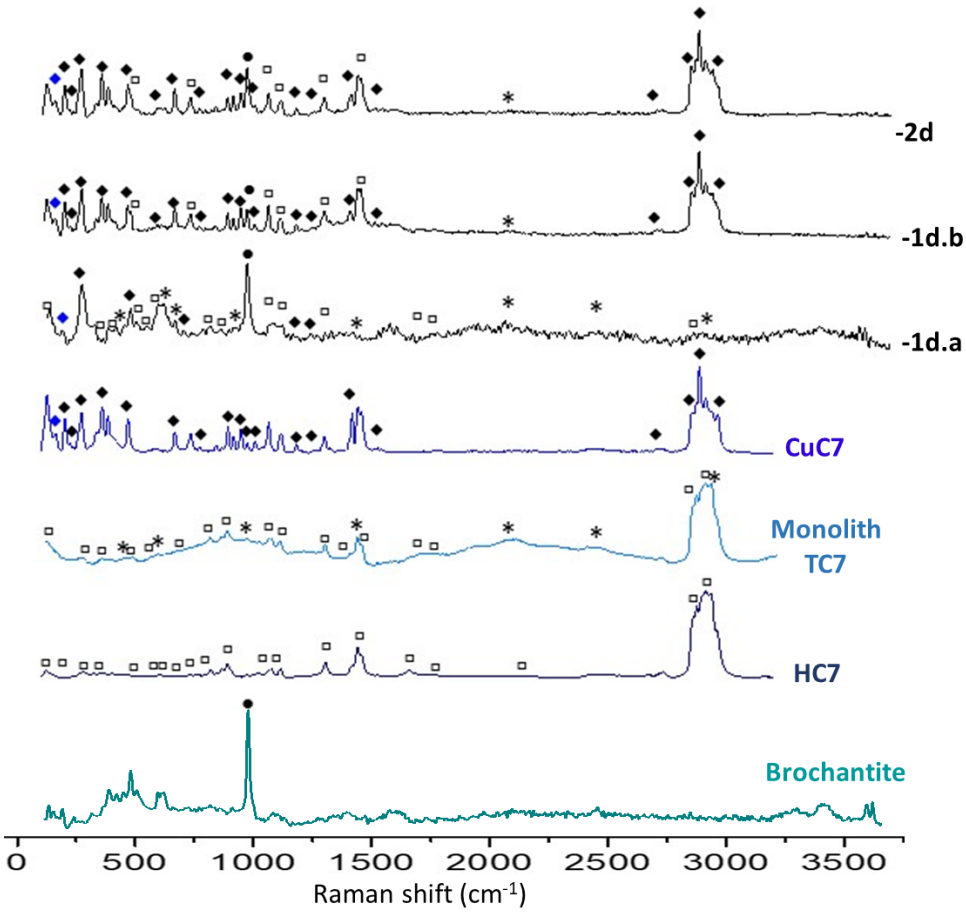

Figure A. 21: normalized Raman spectra from the surface of TC7-coated coupon, -1d (-1d.a and -1d.b) and -2d, showing the presence of copper carboxylate CuC7, by comparison with TC7 monolith (*), HC7 (▫) and CuC7 (▪, ▪).

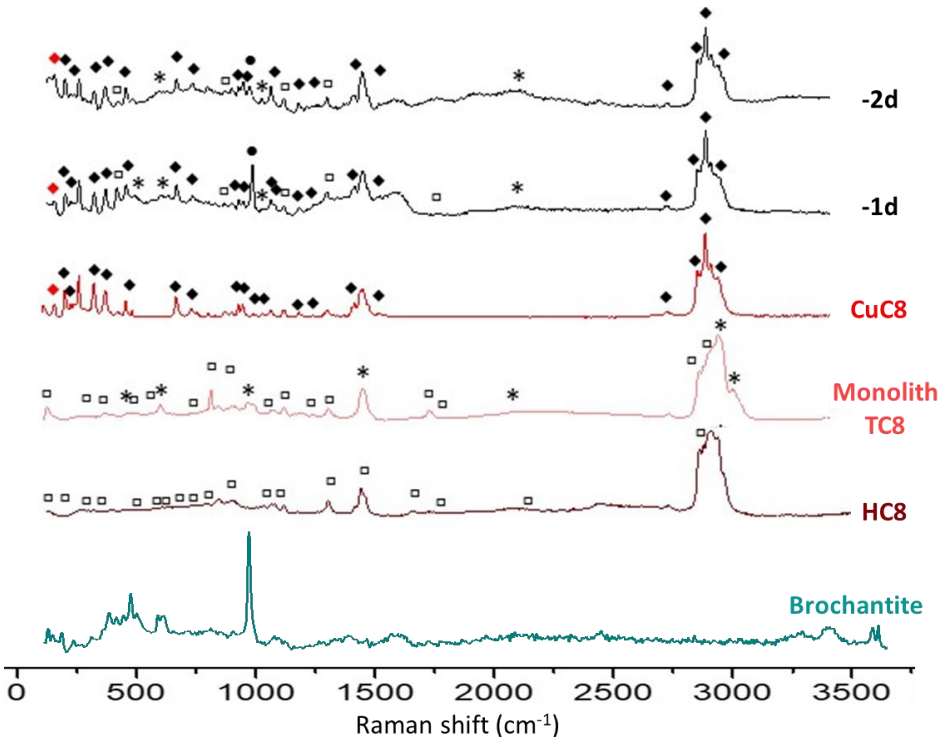

Figure A. 22: normalized Raman spectra from the surface of TC8-coated coupon, -1d and -2d, showing the presence of copper carboxylate CuC8, by comparison with TC8 monolith (*), HC8 (▫) and CuC8 (▪, ▪).

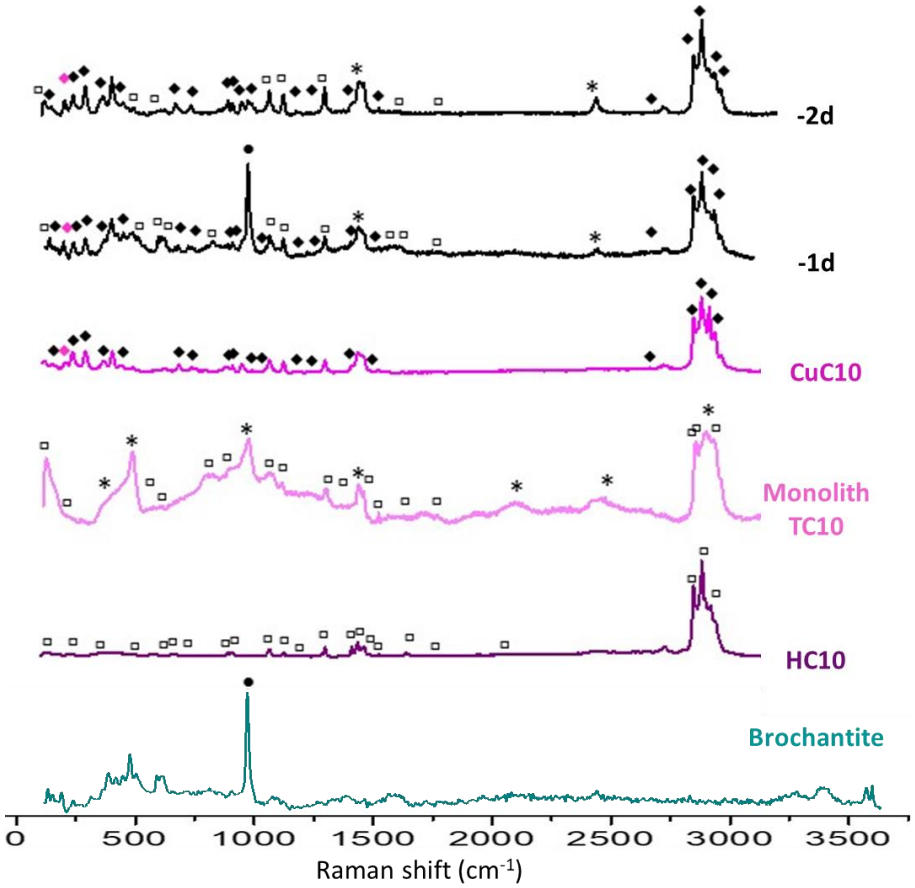

Figure A. 23 : normalized Raman spectra from the surface of TC8-coated coupon, -1d and -2d, showing the presence of copper carboxylate CuC10, by comparison with TC10 monolith (*), HC10 (▫) and CuC10 (▪, ▪).

Appendix B

The EDX and Raman analyses conducted on the TMOS-1d and TMOS-2d coupons are presented in Appendix B, Table B.1 and Fig.B.1. They revealed the presence of Silica at the surface as shown by the higher concentration of Si and Si/Cu ratio comparing the TMOS-coated coupon to the untreated one (Table B.1). these Results showed that no traces of CuCn were found as demonstrated by the Raman spectra from the surface of the TMOS-coated coupon that presented only markers specific of the TMOS monolith reference and the copper substrate itself (Fig.B.1).

Table B. 8 : cc EDS elementary mass composition (relative wt%) from the surface of the TMOS-coated coupon, -1 and -2-dip-coatings for an acquisition area of 130x130 µm², showing the Si/Cu ratio indicating the presence Silica at the surface.

		Coupon + TMOS	
	Untreated coupon	*1d-*	*2d-*
	Relative mass %	Relative mass %	
Cu	45	35	2
S	5	4	0,3
O	37	39	52
Si	0,1	10	34
C	13	11	22
Si/Cu	0,0	0,3	15,5

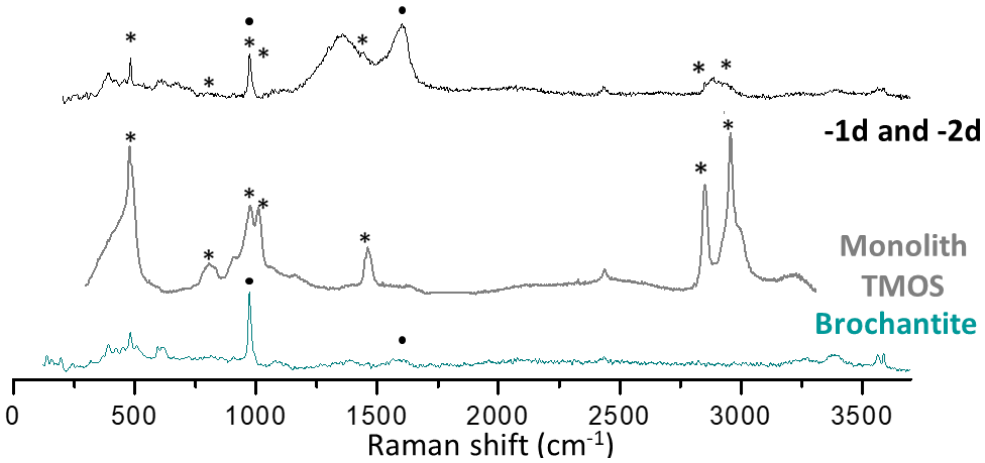

Figure B.1: normalized Raman spectra from the surface of TMOS-coated coupon, -1d and -2d, showing the presence of silica-based material, by comparison with TMOS monolith (*).

Appendix C

Porosity measurements carried out on TCn monoliths enabled us to obtain information on the specific surface area and pore volume of TCn xerogels, presented in this **Appendix C**, Table C.1. The measured pore size is plotted in Figure C.1 to highlight the pore size distribution according to two or three pore family types for each TCn monolith, for measurements carried out at 150°C versus at 50°C (T° for gas desorption before N_2 adsorption/desorption isotherms). The 50°C allows to get the residual porosity of the material while partially preserving the carboxylic acid molecules. The 150°C provides information on the porosity of the TMOS-based matrix after the carboxylic acid evaporation, since the HCn evaporate between 110°C and 144°C under atmospheric pressure. Figure C.1 also shows the percentage of each type of pore family in relation with the total pore volume of the monolith. The table and figure mention the white and the transparent parts of the monolith. This comes from previous results concerning monolith drying, after which we observed both parts. The white part corresponds to the upper part of the monolith after the drying process and is due to the migration and aggregation of HCn molecules during evaporation of the solvents. The transparent part corresponds to the bottom part of the monolith, with lower HCn concentration. Note that this heterogeneous distribution of HCn in the dried monoliths is due its dimensions (1x0,4x4 cm^3 before drying and 0,3x0,1x1,2 cm^3 after drying). The drying process is therefore long, enabling HCn molecules to migrate to the surface with the solvents. In the dipping process, the drying of sub-micrometric and micrometric layers are fast and the HCn molecules are homogeneously distributed in the porous layer.

Table C.1: BET specific surface and porous volume of TMOS, TC7, TC8 and TC10 monoliths, for measurements at 50°C and 150°C

Sample	Temperature (°C)	Specific surface (m2.g-1)	Porous volume (cm3.g-1)
brochantite	150	83±8	0,113±0,011
TMOS monolith	150	556±56	0,268±0,027
TC7 monolith	50	537±54	0,586±0,059
	150	755±76	0,748±0,075
TC8 monolith upper part white	50	175±18	0,538±0,054
	150	271±27	0,66±0,066
TC8 monolith lower part transparent	50	176±18	0,331±0,033
	150	291±29	0,414±0,041
TC10 monolith upper part white	50	_	_
	150	336±34	0,260±0,026
TC10 monolith lower part transparent	50	450±45	0,234±0,023
	150	509±51	0,269±0,027

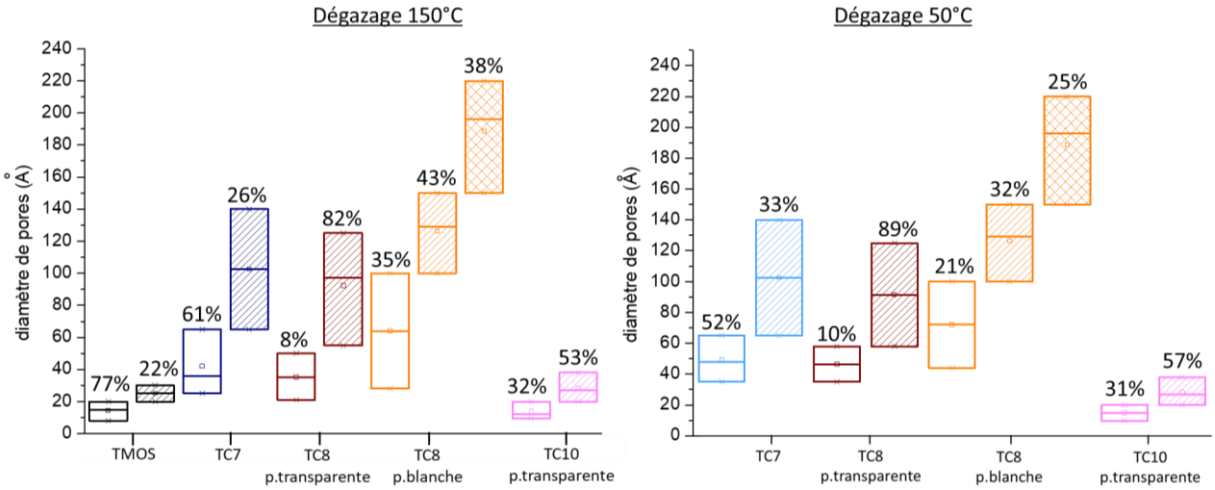

Figure C.24 : pores diameters classified by type of pore-family and monolith type (TMOS, TC7, TC8 and TC10), with the corresponding minimal et maximal values and volume percentage corresponding to each pore-family, for both measurements at 150°C (left diagram) and 50°C (right diagram).

For TC7 TC8 and TC10 monoliths, Figure C.1 shows a similar trend for the results obtained when desorbing gases at 150°C and 50°C under vacuum before carrying out the N_2 adsorption/desorption isotherms. The temperature has very little effect on the pore size distribution thus indicating that the porous network is practically formed before the solvent evaporation and that the acids are trapped in either big or smaller pores in the xerogel network.

Appendix D

The OM images of the TC7 and TC8 cross-section, -1d and -2d, are presented in Appendix D, Fig.D.1 and Fig.D.2. They show a white layer deposited on top of the CL for the -2d's (on the right), indicating the presence of the TMOS-doped coating as presented for the TC10-2d in the article (Fig.8).

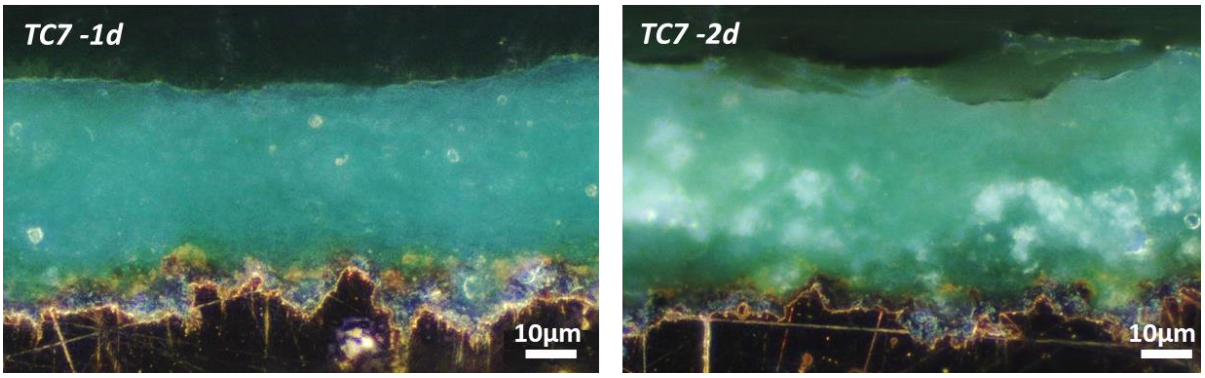

Figure D.1: OM images of the cross section of the TC7 treated coupon, -1d (left) and -2d (right).

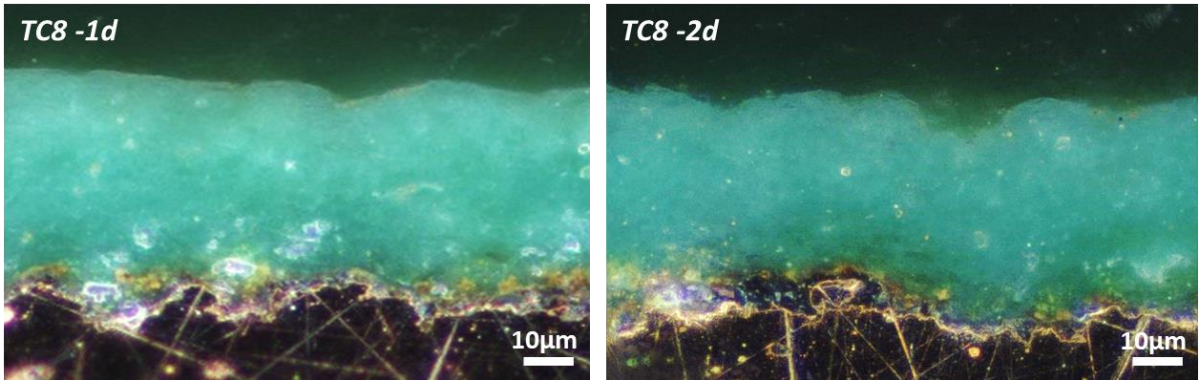

Figure D.2: OM image of the cross section of the TC8 treated coupon, -1d (left) and -2d (right).

Appendix E

The EDS mapping of the TC7 and TC10 coated coupons, -1d and -2d, are presented in Appendix E, Fig.E.1, and Fig.E.2. These results show the presence of Si in the CL along with the additional layer deposited on top of the CL over approximately 2-3 µm for the -2d's. These results confirmed the OMs observation made earlier, concluding on the Si nature of the observed top layer.

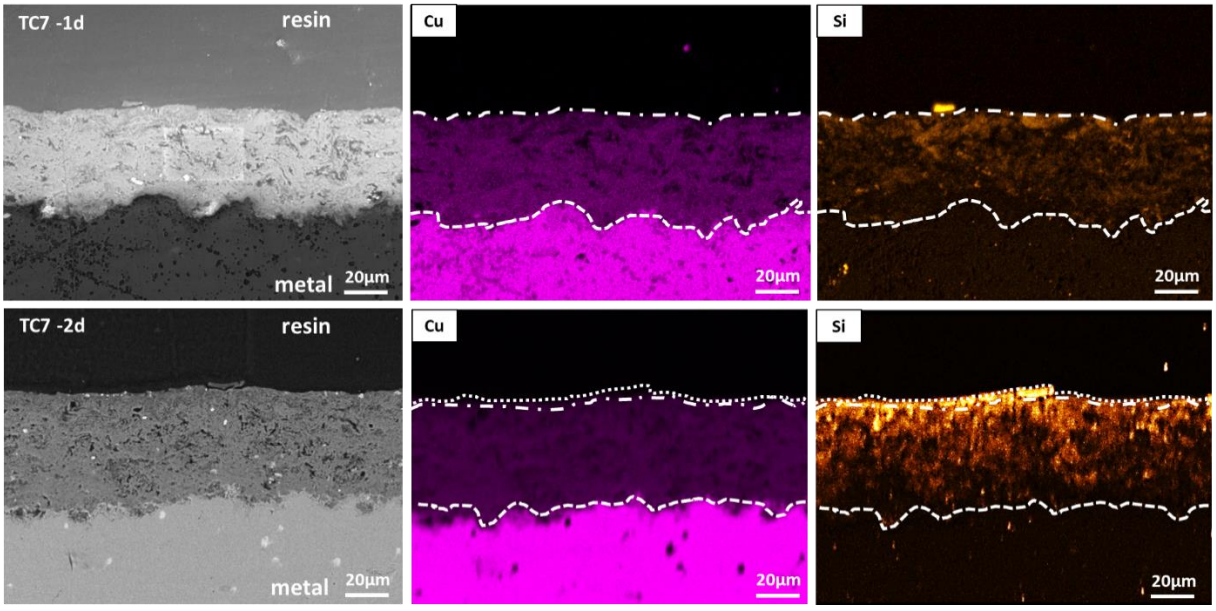

Figure E.1: SEM image (left), Si mapping (centre) and Cu mapping (right) of the TC7 treated coupon cross section, -1d (top) and -2d (bottom).

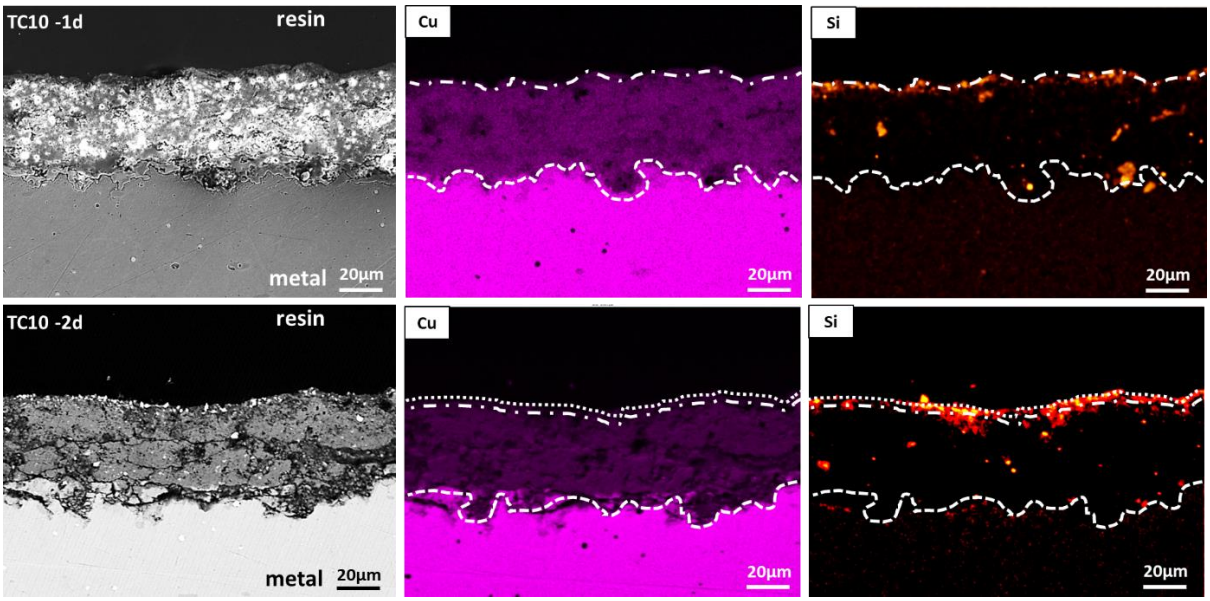

Figure E.2: SEM image (left), Si mapping (centre) and Cu mapping (right) of the TC8 treated coupon cross section, -1d (top) and -2d (bottom).

Appendix F

The Si profiles of the TC7 and TC10 coated coupons, -1d and -2d, are presented in Appendix F, Fig.F.1, and Fig.F.2, displaying the coupon's CL elements, O, S, Cu on the left (relative mass%) and Si from the TMOS-based xerogel on the right (relative mass%) as a function of the depth of penetration into the CL. The figures refer to Z1, Z2, Z3 and Z4 regions as described in the main paper.

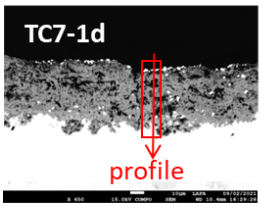

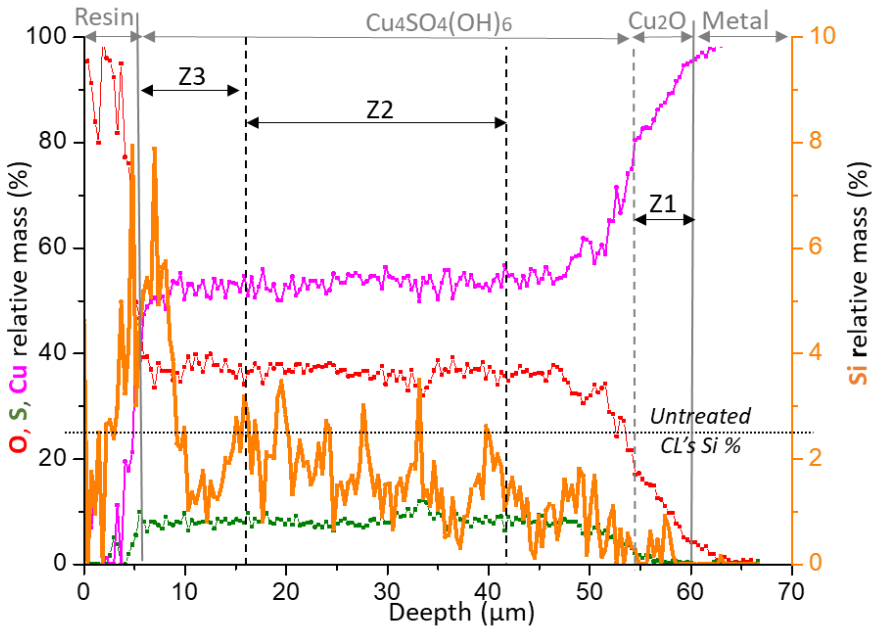

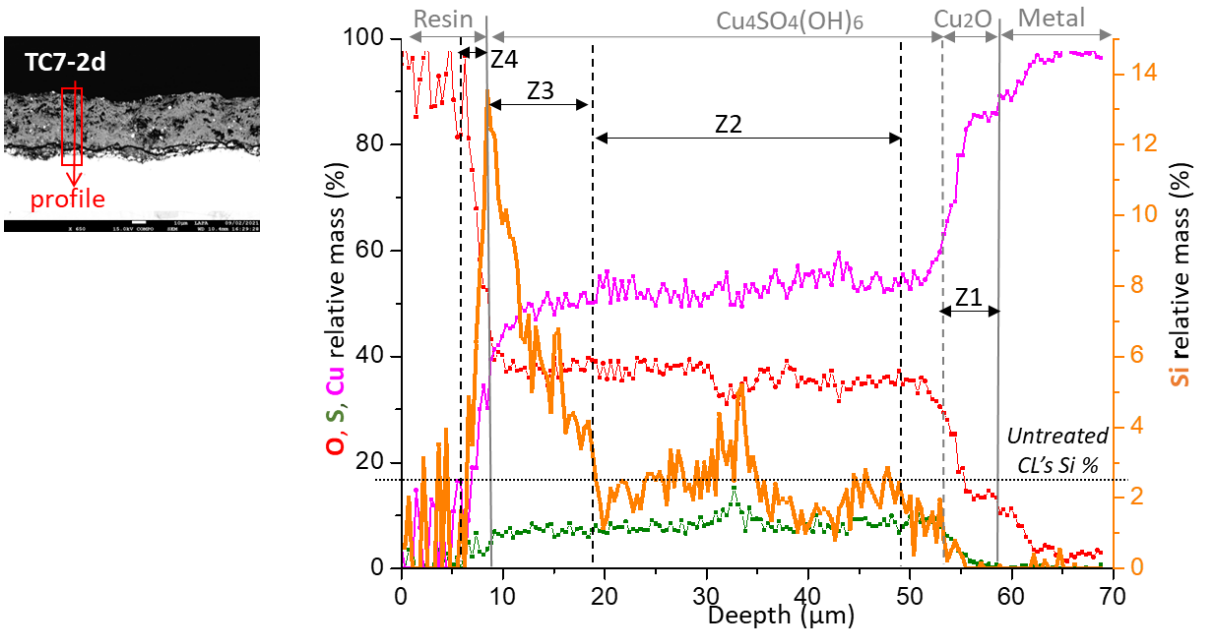

Figure F.1: SEM EDS elemental profile lines for O, S, Cu and Si (scale on right side), in relative mass % correlated to the Si depth penetration in the CL for the cross section of the TC7 coated coupon, -1d (top) and -2d (bottom).

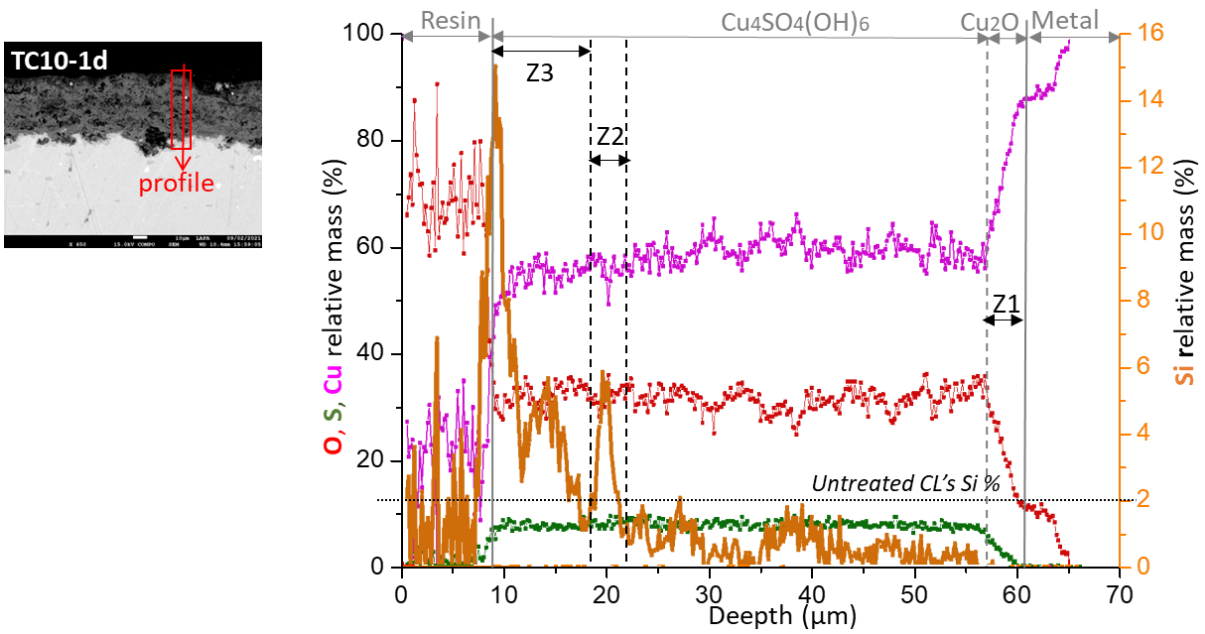

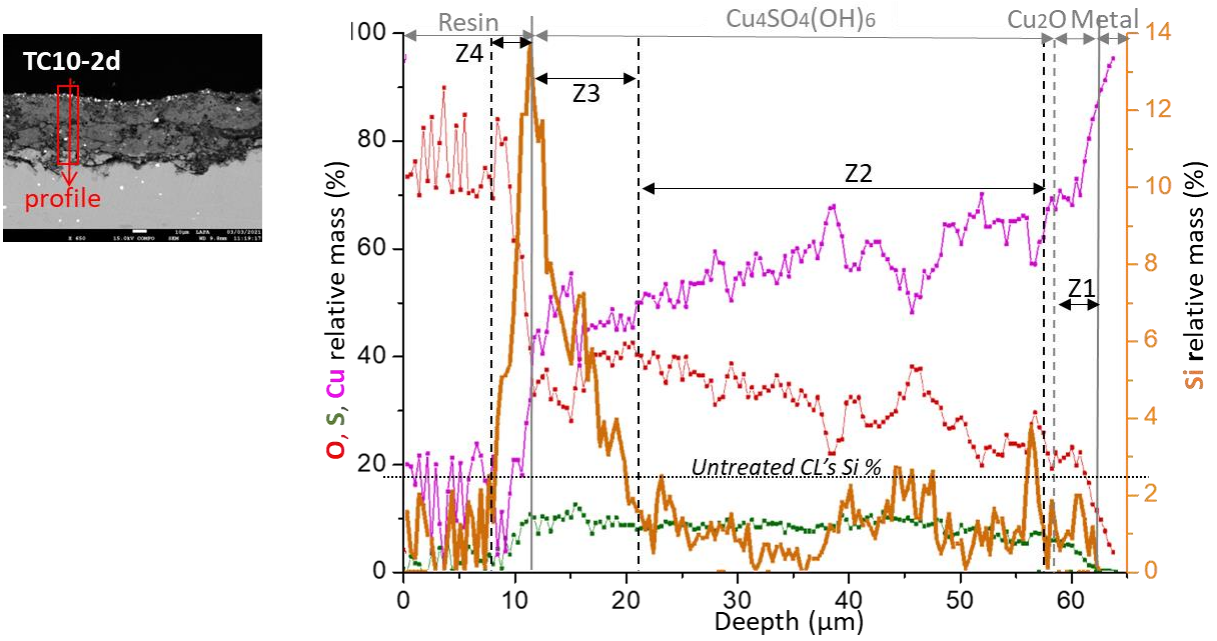

Figure F.2: SEM EDS elemental profile lines for O, S, Cu and Si (scale on right side), in relative mass % correlated to the Si depth penetration in the CL for the cross section of the TC10 coated coupon, -1d (top), -2d (bottom).